

The double sub-giant branch of NGC 6656 (M22): a chemical characterization [★]

A. F. Marino¹, A. P. Milone^{2,3}, C. Sneden⁴, M. Bergemann¹, R. P. Kraft⁵, G. Wallerstein⁶, S. Cassisi⁷, A. Aparicio^{2,3}, M. Asplund^{1,8}, R. L. Bedin⁹, M. Hilker¹⁰, K. Lind¹, Y. Momany¹¹, G. Piotto¹², I. U. Roederer¹³, P. B. Stetson¹⁴, M. Zoccali¹⁵

¹ Max-Planck-Institut für Astrophysik, Karl-Schwarzschild-Str. 1, 85741 Garching bei München, Germany
e-mail: amarino, mbergema, klind@MPA-Garching.MPG.DE

² Instituto de Astrofísica de Canarias, E-38200 La Laguna, Tenerife, Canary Islands, Spain
e-mail: milone, aparicio@iac.es

³ Department of Astrophysics, University of La Laguna, E-38200 La Laguna, Tenerife, Canary Islands, Spain

⁴ Department of Astronomy and McDonald Observatory, The University of Texas, Austin, TX 78712, USA
e-mail: chris@verdi.as.utexas.edu

⁵ UCO/Lick Observatory, Department of Astronomy and Astrophysics, University of California, Santa Cruz, CA 95064, USA
e-mail: kraft@ucolick.org

⁶ Department of Astronomy, University of Washington, Seattle, WA 98195, USA
e-mail: wall@astro.washington.edu

⁷ INAF-Osservatorio Astronomico di Teramo, Via M. Maggini, 64100 Teramo, Italy
e-mail: cassisi@oa-teramo.inaf.it

⁸ Research School of Astronomy & Astrophysics, Australian National University, Mt Stromlo Observatory, via Cotter Rd, Weston, ACT 2611, Australia
e-mail: martin@mso.anu.edu.au

⁹ INAF-Osservatorio Astronomico di Padova, Vicolo dell'Osservatorio 5, 35122 Padova, Italy
e-mail: luigi.bedin@oapd.inaf.it

¹⁰ European Southern Observatory, Karl-Schwarzschild-Str. 2, 85748 Garching bei München, Germany
e-mail: mhilker@eso.org

¹¹ European Southern Observatory, Alonso de Cordova 3107, Santiago, Chile
e-mail: ymomany@eso.org

¹² Dipartimento di Astronomia, Università di Padova, Vicolo dell'Osservatorio 3, Padova, I-35122, Italy
e-mail: giampaolo.piotto@unipd.it

¹³ Carnegie Observatories, 813 Santa Barbara Street, Pasadena, CA 91101 USA
e-mail: iur@obs.carnegiescience.edu

¹⁴ Herzberg Institute of Astrophysics, National Research Council Canada, 5071 West Saanich Road, Victoria, BC V9E 2E7
e-mail: Peter.Stetson@nrc-cnrc.gc.ca

¹⁵ Pontificia Universidad Católica de Chile, Departamento de Astronomía y Astrofísica, Casilla 306, Santiago 22, Chile
e-mail: mzoccali@astro.puc.cl

Received Xxxx xx, xxxx; accepted Xxxx xx, xxxx

ABSTRACT

We present an abundance analysis of 101 subgiant branch (SGB) stars in the globular cluster M22. Using low resolution FLAMES/GIRAFFE spectra we have determined abundances of the neutron-capture strontium and barium and the light element carbon. With these data we explore relationships between the observed SGB photometric split in this cluster and two stellar groups characterized by different contents of iron, slow neutron-capture process (*s*-process) elements, and the α element calcium, that we previously discovered in M22's red-giant stars. We show that the SGB stars correlate in chemical composition and color-magnitude diagram position: the stars with higher metallicity and relative *s*-process abundances define a fainter SGB, while stars with lower metallicity and *s*-process content reside on a relatively brighter SGB. This result has implications for the relative ages of the two stellar groups of M22. In particular, it is inconsistent with a large spread in ages of the two SGBs. By accounting for the chemical content of the two stellar groups, isochrone fitting of the double SGB suggests that their ages are not different by more than ~ 300 Myr.

Key words. globular clusters: general – globular clusters: individual: NGC 6656 – stars: population II – stars: abundances – techniques: spectroscopy

1. Introduction

Thanks to the large amount of spectroscopic and photometric data assembled in the last couple of decades, the assumption that all globular clusters (GCs) contain a simple mono-metallic

Send offprint requests to: A. F. Marino

[★] Based on data collected at the European Southern Observatory with the FLAMES/GIRAFFE spectrograph.

stellar population must be modified. Nearly all GCs stars exhibit substantial star-to-star variations in light elements, mainly C, N, O, Na, Mg, and Al (e.g., Kraft 1994; Ramírez & Cohen 2002; Gratton et al. 2004). These anomalous abundances appear to be present in stars of all evolutionary states, including convectively unmixed subgiant branch (SGB) and main-sequence turnoff stars. This argues that many of the variations were in the birth material of the stars we see today. The light element abundances have various correlations and anticorrelations that point unmistakably to hot H-burning ON, NeNa, and MgAl proton-capture chains. These cannot be products of the present low mass GC stars, so it is probable that a fraction of GC stars are made up of material processed through higher mass stars that are now compact objects in the GCs. Thus multiple stellar generations in GCs are needed (e.g., Marino et al. 2008, Carretta et al. 2009).

In clusters that we may call *normal GCs*, stellar abundances of elements heavier than those affected by H-burning show both intra- and inter-cluster consistency, and their abundances resemble the halo field compositions at similar overall metallicities. For these GCs a two-generation model is sufficient: a primordial generation similar to the field, and stars formed as second generation(s) enriched in material processed through hot H-burning. Powerful photometric tools to separate these stellar generations along the RGBs include the Johnson *U* band and specific Strömgen indices (Marino et al. 2008; Yong et al. 2008). The accepted cluster evolutionary scenario is that *normal GCs* have been polluted with hot H-burning products by first generation asymptotic giant branch stars (AGB, Ventura et al. 2001; D’Antona & Caloi 2004), and/or fast rotating massive stars (Decressin et al. 2007). Massive binaries have also been proposed as an alternative source (de Mink et al. 2009; Vanbeveren, Mennekens & De Greve 2011). Stars formed as second generation members were born from the material released by these proposed first-generation polluters.

Recent spectroscopic studies have revealed that some GCs have variations not only in light elements, but also in the bulk heavy element content. These clusters, which we will designate *anomalous GCs* (AGCs), have significant metallicity dispersions (star-to-star variations in Fe-peak abundances). GCs that have displayed this anomalous behavior include NGC 6656 (M22, Marino et al. 2009), NGC 2419 (Cohen et al. 2010), Terzan 5 (Ferraro et al. 2009), and NGC 1851 (discovered by Yong & Grundahl 2008, and confirmed by Carretta et al. 2010, 2011). All these objects share superficial similarities with the most massive GC ω Centauri, whose huge metallicity variations have been known since the 1970s (e.g. Dickens & Wooley 1967; Freeman & Rodgers 1975; and more recently Norris & Da Costa 1995; Suntzeff & Kraft 1996; Johnson & Pilachowski 2010; Marino et al. 2011b). Omega Cen shows a very broad metallicity distribution that could be consistent with 5-6 groups of stars with different metallicity, as both spectroscopic and photometric studies seem to suggest (Johnson & Pilachowski 2010; Marino et al. 2011b; Sollima et al. 2005; Bellini et al. 2010). The ω Cen metallicity spread is so large that it may have a different origin with respect to the other GCs. It could be the surviving nucleus of a dwarf galaxy tidally disrupted by the Milky Way, as suggested by Bekki & Norris (2006). Differently from the simple *normal GCs*, in these objects successive generation(s) may need to be invoked, with supernovae also playing a role in the pollution of intra-cluster medium.

In the AGCs NGC 1851 and M22, different groups of stars with different slow-process (*s*-process) element abundances have been identified (Yong & Grundahl 2008 for NGC 1851, and Marino et al. 2009, 2011a for M22, hereafter M09 and M11a re-

spectively). Multiple stellar groups in M22 and NGC 1851 are also clearly manifest by a split in their SGB color-magnitude diagram domains, as revealed by Hubble Space Telescope (*HST*) images (Milone et al. 2008; M09; Piotto 2009). The split SGB in these two clusters appears to be related to chemical differences observed among their red-giant branch (RGB) stars.

The chemical complexities in M22 RGB stars have been extensively studied by M09 and M11a. They show that this cluster hosts two metallicity groups, with mean abundances $\langle[\text{Fe}/\text{H}]\rangle = -1.82$ ($\sigma = 0.07$) and -1.67 ($\sigma = 0.05$). These two metallicity groups are characterized principally by different relative contents of the *n*-capture elements that can be efficiently synthesized in the *s*-process. That is, $\langle[\text{Y,Zr,Ba,La,Nd/Fe}]\rangle = -0.01$ ($\sigma = 0.06$) in the lower metallicity group, and $+0.35$ ($\sigma = 0.06$) in the high metallicity group. On the other hand Eu, which predominantly is synthesized in the *r*-process, exhibits constant relative abundances, within the observational errors: $\langle[\text{Eu/Fe}]\rangle = +0.49$ ($\sigma = 0.05$) and $+0.42$ ($\sigma = 0.08$) in the lower and higher metallicity groups, respectively. This clearly indicates that the higher *n*-capture element content in the higher metallicity M22 RGB stars is due to addition of material produced via the *s*-process. The two stellar groups were named *s*-rich and *s*-poor by M09, and we will follow that convention here.

For M22, M09 also demonstrated that stellar models cannot entirely reproduce the size of the SGB photometric split by considering only its metallicity spread. They suggested that the origin of the split could be more complex, and involve also difference in age and/or variations in the total CNO abundance, as proposed by Cassisi et al. (2008) and Ventura et al. (2009) for NGC 1851. This scenario is supported by observational evidence for total C+N+O variations among RGB stars both in NGC 1851 (Yong et al. 2009), and M22 (M11a).

Although photometric evidence for the population multiplicity of M22 is most clearly evident in the SGB domain, previous detailed abundance studies have been carried out only for the brighter RGB and AGB stars. In this study we eliminate this sample mismatch by performing a chemical composition analysis of 101 SGB stars in M22. The layout of this paper is as follows: §2 is an overview of the data set; §3 contains a description of model atmospheres and abundance derivations; §4 presents the abundance results, that are discussed in §5 and §6. The findings of this paper are summarized in §7.

2. Observations and data reduction

Basic information for M22 can be found in Harris (1996)¹. At a distance of ~ 3.2 kpc M22 is one of the GCs closest to the Sun. It has an half-light radius of $3.36'$ and a mass of $\log \frac{M}{M_{\odot}} \sim 5.5$, as listed in Mandushev et al. (1991). In this section we consider in turn the photometric and spectroscopic data that we have employed in this study.

2.1. The photometric dataset

We first establish that the SGB of M22 is photometrically split in a manner that mimics the division already established among the RGB (M11a). We then consider three distinct sets of photometry available in the literature, in order to investigate the distribution of spectroscopic targets in the color-magnitude diagram (CMD). Ground-based observations were used to analyze the CMD over a wide spatial field in the *B* and *V* bands, and to estimate the

¹ The 2010 updated version of the Harris catalog is available at <http://www.physics.mcmaster.ca/~harris/mwgc.dat>

atmospheric parameters of the spectroscopic targets. In addition, we used ground-based U images available for a smaller field, and images taken with the Advanced Camera for Surveys on board the Hubble Space Telescope (*ACS/HST*; Clampin et al. 2002 and references therein) in the F606W and F814W bands to make our study of the double SGB extend from the ultraviolet to the infrared spectral regions.

The *HST ACS/WFC* images were obtained under program GO-10775 (PI Sarajedini). The data sets consist of (short exposure, deep exposures) = 3s, 4×55s in F606W, and 3s, 4×65s in F814W. We used the photometric catalogs provided by Anderson et al. (2008) reduced as described in Anderson & King (2006).

The ground-based photometric database consists of a total of 533 individual CCD images taken at different telescopes (see Tab. 1). These images were taken as part of P. B. Stetson’s program to produce a large homogeneous globular cluster database. The images were reduced and calibrated as described in detail by Stetson (2000, 2005). The final photometric catalog covers a total field of view of $\sim 34' \times 33'$ and contains 730,432 entries; of these, 604,979 objects had sufficient data to allow calibration in at least V and one other filter. We used the B and V magnitudes from this catalog.

In addition to this wide field catalog, we used a separate photometric catalog derived from images collected by the Superb-Seeing Imager (SUSI2) camera, previously mounted on ESO-NTT telescope (Tab. 1). The SUSI2 camera was a mosaic of two $2k \times 4k$, $0'.085$ pixel CCDs, where each chip covered a field of view of $5'.5 \times 2'.7$. The photometric reduction and calibration of this data-set was presented in Momany et al. (2004). In this catalog, U and V magnitudes are available.

Since we were interested only in target stars with high-accuracy photometry, we included in our analysis only relatively isolated stars with good values of PSF-fit quality indices and small errors in photometry and astrometry. A detailed description of the selection procedures is given in Milone et al. (2009).

M22 has an average reddening $E(B - V) = 0.34$ (Harris 1996); such a large reddening value is rarely uniform over a cluster face. Corrections for differential reddening applied to the HST GC dataset is discussed in detail by Piotto et al. (2012) for the case of M22. To account for the color and magnitude differences that differential reddening produces in the ground-based CMDs, we used the procedure described by Milone et al. (2011). In brief, we first drew a main-sequence ridge (fiducial) line by putting a best-fit spline through the median colors found in successive short intervals of magnitude. We iterated this step with an outlier sigma clipping. Then for each program star, we estimated how much the observed stars in its spatial vicinity systematically lie to the red or the blue of the fiducial sequence. This systematic color and magnitude offset, measured along the reddening line, is indicative of the local differential reddening.

We corrected for differential reddening all of the *HST* and ground-based color-magnitude diagrams used in this paper. As an example, in Fig. 1, we compare the original (panel *a*) and the corrected U -($U - V$) CMD (panel *b*) of M22 for the SUSI2@NTT photometry from Momany et al. (2004). The choice of this combination of magnitude and color is due to its ability to separate photometric sequences at different evolutionary stages along the CMD. The blue and near- UV regimes of cool-star spectra contain many CH and CN molecular features. Stars with different amounts of these elements populate different RGB sequences in CMDs constructed by using the U -band (Marino et al. 2008).

Inspection of Fig. 1 shows that after the differential reddening correction has been applied, many features of the CMD became narrower and more clearly defined. To better demonstrate the quality of this correction we performed some tests represented in the lower panels of Fig. 1. We drew by hand the fiducials for the brighter SGB and bluer RGB population, and superimposed them to the CMDs as red dashed-dotted lines. For each RGB star, we calculated the color difference $\Delta(U - V)$ from the fiducial at a given U magnitude, while for the SGB stars we calculated the difference in the U magnitude at a given color. These color and magnitude differences, as well as histogram plots, have been represented in the lower panels of Fig. 1. The verticalized U versus $\Delta(U - V)$ diagram is plotted in panels *c* and *d* for RGB stars with $17.5 < U < 19.4$ by using original and corrected photometry respectively. The corresponding histogram color distributions are shown in panels *e* and *f*.

Panels *g* and *h* of Fig. 1 show the $(U - V)$ versus ΔU diagram for SGB stars with $2.90 < (U - V) < 3.15$ obtained from original and corrected magnitudes respectively. The corresponding histogram color distributions are plotted in panels *i* and *l*. The better separation of the SGB and RGB sequences in the corrected diagram suggests that differential reddening has been substantially removed. Our differential reddening correction shows that the maximum values of $\Delta E(B - V)$ are approximately of 0.1 mag across the face of the cluster.

Examination of the reddening-corrected U versus $(U - V)$ diagram (panel *b*) of Fig. 1 clearly reveals that the bright SGB is connected to the blue RGB, while red RGB stars are the progeny of the faint SGB. We anticipate that this connection between the two SGBs and RGBs would be further confirmed by our M22 SGB investigation, and we will explore these relationships in §5.

2.2. The spectroscopic dataset

Our spectroscopic data consist of a large number of FLAMES/GIRAFFE spectra (Pasquini et al. 2002, 2003) observed under the program 085.D-0698A (PI: Marino). The low resolution LR02 GIRAFFE setup was employed, which covers a spectral range of $\sim 600 \text{ \AA}$ from 3964 \AA to 4567 \AA , and provides a resolving power $R \equiv \lambda/\Delta\lambda \sim 6,400$. All our target stars were observed in the same FLAMES plate in four different exposures of 46 minutes plus one exposure of 26 minutes, for a total observing time of 210 minutes. The typical S/N of the fully reduced combined spectra is ~ 90 -100 at the central wavelength of the spectral range. Data reduction involving bias-subtraction, flat-field correction, wavelength-calibration, sky-subtraction, has been done by using the dedicated pipeline BLDRS v0.5.3².

In total we gathered spectra for 109 candidate M22 SGB stars. The M22 SGB stars lie in a $(B - V)$ color region ranging from ~ 0.8 to ~ 1 , and extend in V magnitude from ~ 17.8 up to ~ 16.7 . Cluster membership of the stars was established from the radial velocities obtained using the IRAF@FXCOR task, which cross-correlates the object spectrum with a template. For the template we used a synthetic spectrum obtained through the spectral synthesis code SPECTRUM (Gray & Corbally 1994)³. This spectrum was computed with a model stellar atmosphere interpolated from the Kurucz (1992) grid⁴, adopting parameters $(T_{\text{eff}}, \log g, \xi_t, [\text{Fe}/\text{H}]) = (6000 \text{ K}, 3.5, 1 \text{ km s}^{-1}, -1.70)$.

² See <http://girbl-d-rs.sourceforge.net>

³ See <http://www.phys.appstate.edu/spectrum/spectrum.html> for more details.

⁴ <http://kurucz.harvard.edu/grids.html>

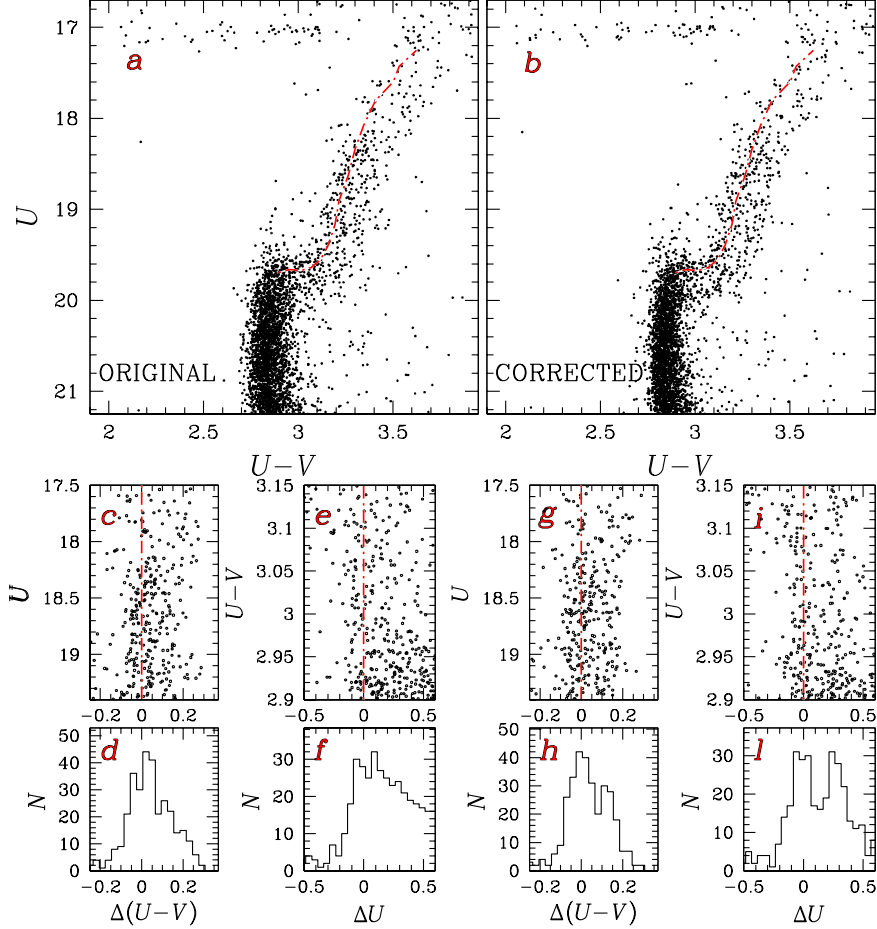


Fig. 1. Comparison of the U versus $(U - V)$ CMD from NTT photometry (Momany et al. 2004) before (panel *a*) and after (panel *b*) the correction for differential (but not for the absolute) reddening. The horizontal branch stars lie at $U \sim 17$. The $\Delta(U - V)$ distributions of RGB stars with respect to the fiducial (red-dotted line on the CMDs) are shown in panels *c* and *d* for the non-corrected CMD, and in panels *g* and *h* for the corrected one. For SGB stars we show the distributions of the ΔU magnitude relative to the fiducial shown in the CMDs for the non-corrected (panels *e* and *f*) and the corrected (panels *i* and *l*) CMDs.

Observed radial velocities were corrected to the heliocentric system. The observed/template spectrum matches, after the heliocentric correction, yielded for the whole sample a mean radial velocity of $-143 \pm 1 \text{ km s}^{-1}$ ($\sigma = 9 \text{ km s}^{-1}$). This value is in reasonable agreement with the values in the literature (e.g., $-148.8 \pm 0.8 \text{ km s}^{-1}$, $\sigma = 6.6 \text{ km s}^{-1}$, Peterson & Cudworth 1994; $-146.3 \pm 0.2 \text{ km s}^{-1}$, $\sigma = 7.8 \text{ km s}^{-1}$, Harris 1996). Then we rejected individual stars with values deviating by more than 3σ from this average velocity, deeming them to be probable field stars. After the rejection of these field stars, our sample of *bona fide* cluster stars is composed of 101 SGBs.

Basic $UBVI$ photometry for the M22 spectroscopically analyzed stars is listed in Tab. 2. In this table we list the coordinates, the original U , B , V , and I magnitudes from the ground-based photometry, and the differential reddening correction $\Delta E(B - V)$ applied to each target.

3. Data analysis

3.1. Atmospheric parameters

Chemical abundances were derived from a local thermodynamic equilibrium (LTE) analysis by using the latest version of the spectral analysis code MOOG (Snedden 1973).⁵

Effective temperatures (T_{eff}) were estimated by using the Casagrande et al. (2010) $(B - V)$ - T_{eff} calibrations (based on the “infrared flux method”) for main sequence and subgiant stars. Our colors were corrected for the mean M22 reddening after accounting for differential reddening effects as described in Sect. 2.1. Indeed, as discussed in Casagrande et al., accurate reddening corrections are crucial in determining T_{eff} via the infrared flux method: a shift of only $+0.01 \text{ mag}$ in $E(B - V)$ translates into a T_{eff} change of about $+50 \text{ K}$. In the case of M22, differential reddening effects are quite large, and, if left uncorrected, would yield $(B - V)$ -based T_{eff} errors up to $\sim 500 \text{ K}$. After applying the differential reddening corrections, we estimate that our internal color uncertainties are ≈ 0.01 - 0.015 mag , implying

⁵ Available at <http://www.as.utexas.edu/~chris/moog.html>

internal uncertainties of ~ 100 K in T_{eff} . Of course, some stars in our sample, mainly those in the central crowded field of the cluster where the ground-based photometry is not good, have larger photometric errors. For these stars we expect to have larger errors in the colors that translate into larger internal errors in the derived temperatures.

Surface gravities ($\log g$) were obtained from the apparent V magnitudes, the above T_{eff} , assuming a mass $M = 0.80M_{\odot}$, bolometric corrections from Alonso et al. (1999), and an apparent distance modulus of $(m - M)_V = 13.60$ (Harris 1996, 2010 updated). This value agrees with the one obtained by our best isochrone-fit value, $(m - M)_V = 13.64$ (Piotto et al. 2012). Gravities derived in this manner are affected mainly by the adopted distance modulus and mass, whose variations systematically change the surface gravities. An internal variation of ~ 0.1 in the adopted stellar masses modifies $\log g$ values of ~ 0.05 dex, with lower gravities for lower masses. Such minor excursions in $\log g$ do not affect significantly the abundances derived in this paper (see the error analysis in Sect. 3.2). The derived values for T_{eff} and $\log g$ are listed in Tab. 3. They span a range of ~ 900 K and ~ 0.70 , respectively.

Microturbulent velocities cannot be independently determined from our spectra or photometry, so we adopted the Gratton, Carretta & Castelli (1996) prescription:

$$\xi_t = 2.22 - 0.322 \times \log g \quad (1)$$

However, since all our SGB stars have similar gravities this relation predicts very similar ξ_t values, with a mean $\langle \xi_t \rangle = 0.97 \pm 0.01 \text{ km s}^{-1}$ ($\sigma = 0.04$). Therefore we assumed a uniform microturbulence of 1.0 km s^{-1} for all our targets.

For the metallicity of our model atmospheres we used in a general way the results of M09 and M11a, derived from their analysis of high resolution spectra of a large sample of RGB stars. Those papers demonstrated that M22 hosts two groups of stars, one which is s -rich and one which is s -poor, with different metallicities by a mean $[\text{Fe}/\text{H}]$ variation of ~ 0.15 dex. The different metallicities are accompanied by large difference in s -process elemental abundances, with the s -rich stars having higher metallicity with respect to the s -poor stars. Given the relatively low resolution of our spectra, it is very difficult to detect such small metallicity variations in our SGB program stars. A difference of 0.15 dex in metallicity does not lead to significant departures in the relevant model atmosphere quantities (such as opacity). Nevertheless, in our analysis we have accounted for this difference by using the following procedure. (i) First we adopted the mean metallicity of the cluster, $[\text{A}/\text{H}] = -1.76$ (M09 and M11a), as the metallicity for a given star. (ii) Then we derived the stars's abundance of Sr, an element whose abundance in the Solar system is predominantly produced by the s -process. (iii) Having then an estimate of the s -process content of each star, we adopted in its final model atmospheres the mean metallicity obtained in our previous work for the s -rich and s -poor stars: $[\text{A}/\text{H}] \approx -1.67$ for the s -rich stars, and $[\text{A}/\text{H}] \approx -1.82$ for s -poor ones (see their Tab. 7).

In Fig. 2 we show two averaged spectra, covering three Fe I lines, obtained from a sample of s -rich and s -poor stars (we refer the reader to §4 for more details). On each observed line we have superimposed two synthetic spectra with appropriate atmospheric parameters, but one with $[\text{Fe}/\text{H}] = -1.67$ (the mean metallicity of s -rich stars) represented in red, and the other with $[\text{Fe}/\text{H}] = -1.82$ (the mean metallicity of s -poor stars) represented in blue. The averaged s -poor star is consistent with having a lower metallicity than the s -rich one, and the level of the Fe difference is similar to the one that M09 and M11a found

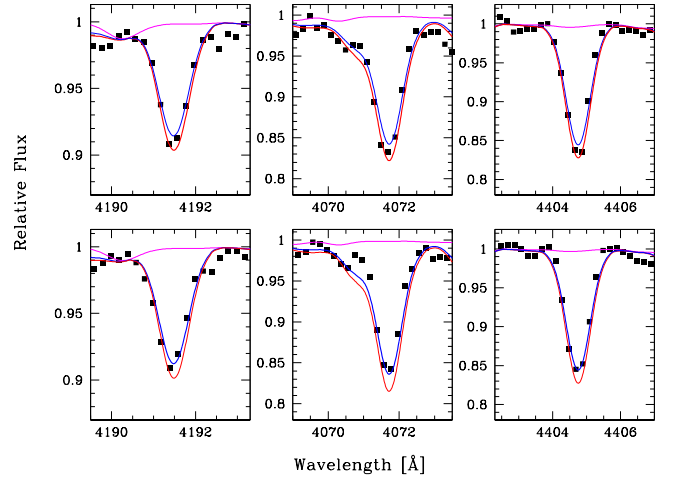


Fig. 2. Fe I lines for the combined s -poor (lower) and s -rich (upper) spectra of Fig. 7. Superimposed on the observed spectra are synthetic spectra corresponding to the $[\text{Fe}/\text{H}] = -1.67$ (red), $[\text{Fe}/\text{H}] = -1.82$ (blue), and with no Fe (magenta).

in RGB stars. However, the line strength differences are small, illustrating the difficulty of determining the small difference in metallicity among s -rich and s -poor SGB stars from our individual spectra.

The contributions to the continuum source function due to Thomson+Rayleigh scattering effects are small at our metallicity-temperature-gravity regime for our spectral lines. Indeed, we verified that the differences in Sr, Ba, and C abundances obtained with the scattering and non-scattering versions of our synthetic spectrum code MOOG are negligible. Therefore, we used the code version that does not take scattering into account.

In order to keep the present analysis consistent with our previous work on M22, we used interpolated model atmospheres from the grid of Kurucz (1992), with fixed T_{eff} , $\log g$, ξ_t , and metallicity. These models were constructed with inclusion of convective overshooting. Our trial syntheses suggest that the use of these models produces an over-estimation of ~ 0.10 dex in all abundances compared with those determined with model atmospheres from Castelli & Kurucz (2004), which do not assume convective overshooting. We emphasize that the metallicity assumptions had little influence on establishing the s -richness of individual stars; these were accomplished almost exclusively by the Sr abundances. More details on the segregation of stars on basis of s -element content are given in §4.1.

3.2. Chemical abundances

Using the model atmospheres and analysis code described in §3.1, we determined abundances for the neutron-capture (n -capture) elements Sr and Ba and for light element C.

Limited by the relatively low resolution and the small wavelength range of our spectra, we derived Sr and Ba abundances only from the strong resonance transitions Sr II 4077, 4215 Å, and Ba II 4554 Å. Both the Sr lines suffer from many blends with other surrounding transitions, mostly Fe features and, in the case of the Sr II 4077, also other n -capture species (Dy and La). Spectral synthesis in the analysis of these lines (and particularly at our moderate resolution) is necessary to take these blends into account. Although the Ba II 4554 Å is isolated from contaminat-

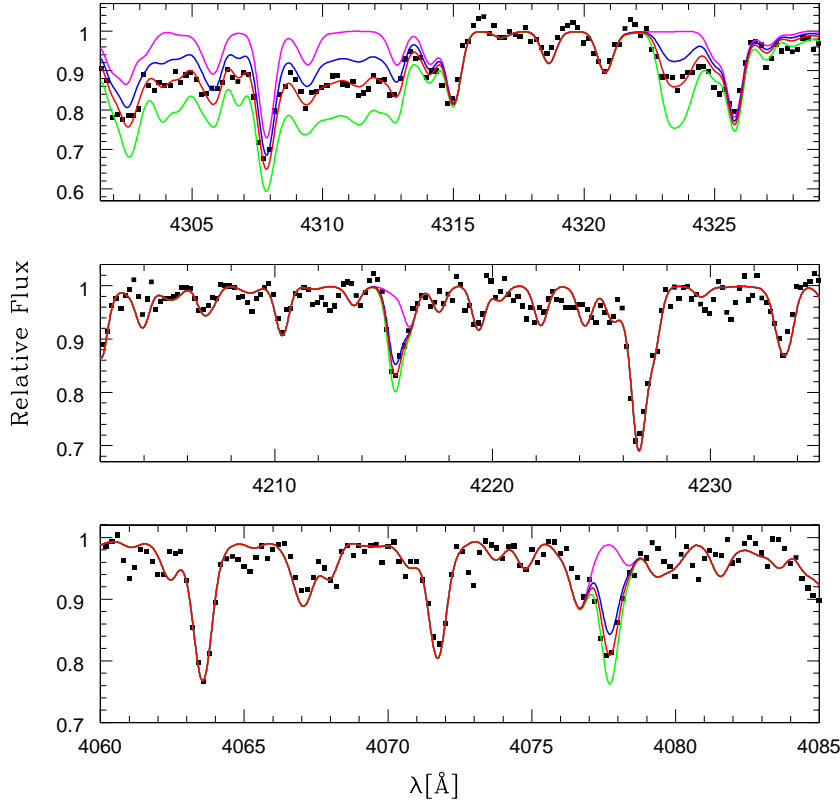


Fig. 3. Observed and synthetic spectra around the Sr lines at 4077 Å and 4215 Å and the G band for the *s*-rich star #2505. In each panel the points represent the observed spectrum, and the continuous lines are the synthesis computed with $[\text{Fe}/\text{H}] = -1.76$ and with different strontium and carbon abundances. The magenta line is the spectrum computed with no contribution from Sr II and C; the red line is the best-fitting synthesis (with the abundances given in Tab. 3); and the green and blue lines are the syntheses computed with Sr and C abundances altered by ± 0.3 dex from the best value.

ing transitions, we computed synthesis also for the Ba spectral line, to take its isotopic splitting into account. The linelists are based on Kurucz line compendium,⁶ apart from the Ba transition for which we added hyperfine structure and isotopic data from Gallagher et al. (2010). For Sr our linelists neglect hyperfine/isotopic splitting; the wavelength shifts are very small and Sr has one dominant isotope.

The resonance lines of Sr II and Ba II are formed relatively far out in the atmosphere, and, according to our NLTE calculations, are affected by departures from LTE (see e.g. Bergemann & Gehren 2008 for details on these calculations). Here, we note that Sr II and Ba II are the majority ions of their elements in the atmospheres of late-type stars (as also demonstrated by Short & Hauschildt 2006), and the major deviations from LTE are due to the non-equilibrium excitation effects in the line transitions. In particular, deviation of the line source functions from the Planck function leads to the NLTE profile strengthening, thus requiring somewhat lower abundances to fit observed spectral lines. For further details on the NLTE effects affecting our lines we refer the reader to Bergemann et al. (to be submitted to A&A). Here, we use these NLTE corrections to estimate how much our abundances could be affected by these effects. According to our NLTE calculations, we estimated NLTE corrections to range from -0.12 to $+0.04$ dex for the Ba II 4554 Å line, and only from -0.05 to 0.00 dex for the two Sr II lines.

An additional difficulty in the analysis of Ba is that it has five major naturally-occurring isotopes whose production fractions

in the rapid-process (*r*-process) and *s*-process are significantly different (e.g., Kappeler et al. 1989). In particular, abundances derived from the Ba II 4554 Å transition are very sensitive to the adopted *r/s* fraction (e.g. Mashonkina & Zhao 2006; Collet et al. 2009). This is an issue in the analysis of M22, which hosts stars with different contribution from the *s*-process material, as demonstrated in M09 and M11a.

The M22 *s*-poor stars have *n*-capture abundance distributions that are compatible with pure *r*-process material, as shown in Roederer et al. (2011). Since the *s*-rich stars should have a larger nucleosynthetic contribution coming from the *s*-processes (recalling that within observational errors, Eu is constant in the two M22 *s*-groups), a two-step abundance analysis needed to be adopted. We first determined Ba abundances by adopting a scaled solar-system Ba abundance and isotopic fractions (Lodders 2003) for all the stars in our sample. Then the initial Sr syntheses were used to divide the total sample into *s*-poor and *s*-rich groups of stars (as discussed further in Sect. 4.1). Finally we recalculated the Ba abundances of the *s*-poor stars, assuming a pure *r*-process isotopic ratio (Arlandini et al. 1999). The re-computed Ba abundances in *s*-poor stars are lower by ~ 0.20 dex than the ones obtained in our first abundance estimates. Of course a similar systematic shift towards lower Ba abundances is obtained also for the *s*-rich stars if a pure *r*-process isotopic ratio is assumed. However, for the *s*-rich stars, we kept our original Ba abundance values, because the solar-system isotopic fractions for the *s*-rich stars appear to be a good approximation. This is justified since M11a showed that the M22

⁶ <http://kurucz.harvard.edu/linelists.html>

s-rich RGB stars have a solar-system *n*-capture-element mix, i.e., [Y,Zr,Ba,La,Nd/Eu] \approx 0.

Carbon was measured from spectral synthesis of the CH ($A^2\Delta - X^2\Pi$) G-band heads near 4314 and 4323 Å. The molecular line data employed for CH were provided by B. Plez (priv. comm.; some basic details of the linelist are given in Hill et al. 2002). As an example, we show in Fig. 2 the spectral synthesis of the Sr lines and the G band for the *s*-rich star #2505 ($T_{\text{eff}} = 5923$ K, $\log g = 3.97$, $[A/H] = -1.67$). A list of the derived chemical abundances, together with the atmospheric parameters, is provided in Table 1.

An internal error analysis was accomplished by varying one by one the temperature, gravity, metallicity, and microturbulence, and re-determining the abundances for three stars spanning the entire range in T_{eff} . The parameters were varied by $\Delta T_{\text{eff}} = \pm 100$ K, $\Delta \log g = \pm 0.2$, $\Delta [Fe/H] = \pm 0.1$, and $\Delta \xi_t = \pm 0.2$, typical uncertainties associated with our atmospheric parameters. The contribution of continuum placement errors was estimated by determining the change in abundances as the synthetic/observed continuum normalization was varied: generally this uncertainty added 0.10 dex to the abundances. The various errors were added in quadrature, resulting in typical uncertainties of ≈ 0.15 for the C abundances, ≈ 0.25 for the individual Sr line abundances, and ≈ 0.22 dex for Ba. The standard errors σ associated with the mean Sr abundances obtained from the two available spectral lines, are listed in Tab. 3. The mean of these σ values, that is 0.08 ± 0.01 , is an estimate of the error associated with the mean Sr abundance of each star. Systematic effects could affect our atmospheric parameters, which would lead to systematic abundance differences that could be larger than those introduced by internal uncertainties. However, we are interested here only in relative star-to-star chemical variations among a set of M22 SGB stars with a restricted parameter range. This renders systematic abundance uncertainties unimportant for our purposes. Investigation of such systematics is worth pursuing in the future, but is beyond the aims of our work.

4. RESULTS

Our results for C, Sr, and Ba abundances in all program stars are listed in Tab. 3. These three elements all show a large spread that cannot be entirely accounted for by observational errors. The mean abundances for all the analyzed stars are: $\langle [C/H] \rangle = -1.75$ ($\langle [C/Fe] \rangle = 0.00$, $\sigma = 0.22$, for 100 stars); $\langle [Sr/H]_{\text{NLTE}} \rangle = -1.66$ ($\langle [Sr/Fe]_{\text{NLTE}} \rangle = 0.10$, $\sigma = 0.21$, for 101 stars); and $\langle [Ba/H]_{\text{NLTE}} \rangle = -1.63$ ($\langle [Ba/Fe]_{\text{NLTE}} \rangle = 0.13$, $\sigma = 0.26$, for 100 stars).

For strontium and barium the mean abundances are those corrected for NLTE. In the following we discuss the spreads of each single element.

4.1. Strontium

In Fig. 4 we plot the LTE and NLTE Sr abundances for our program stars, both in “absolute” $\log \epsilon$ units and relative [Sr/Fe] ratios. The large spreads in Sr that we observe here are consistent with our findings on RGB stars. The small NLTE corrections make no significant alterations to these spreads. No Sr abundances were reported in M09 and M11a. However, the Sr distribution for our SGB sample is clearly bimodal, similar to the M22 distributions of many other *n*-capture elements among RGB stars.

In the following, we use the Sr abundances to divide *s*-rich from *s*-poor stars. Our working hypothesis is to consider the stars having $\log \epsilon(\text{Sr}_{\text{LTE}}) > 1.40$ to be *s*-rich, and the ones with $\log \epsilon(\text{Sr}_{\text{LTE}}) \leq 1.40$ to be *s*-poor. The Sr distributions, in the left panel of Fig. 4, illustrate our chosen selection of *s*-rich (red) and *s*-poor (blue) stars. In the right panel we show the two histogram distributions in [Sr/Fe] of the selected *s*-rich and *s*-poor stars, constructed by using for the two groups the mean [Fe/H] values of -1.67 and -1.82 , respectively. The adoption of one [Fe/H] value for the *s*-poor stars and one for the *s*-rich stars does not appear to introduce additional spread to the distributions of the two groups, and the apparent larger spreads for the [Sr/Fe] are only due to small binning effects.

Based on our selection, our sample is composed by 56 *s*-poor and 45 *s*-rich stars. The *s*-poor stars have $\log \epsilon(\text{Sr}) = 1.09 \pm 0.02$ and $\sigma = 0.11$ ($\langle [Sr/Fe] \rangle = -0.06 \pm 0.02$), while the *s*-rich ones have $\log \epsilon(\text{Sr}) = 1.59 \pm 0.02$ and $\sigma = 0.11$ ($\langle [Sr/Fe] \rangle = 0.29 \pm 0.02$). The difference in Sr abundances between the two selected groups is $\log \epsilon(\text{Sr}) = 0.40 \pm 0.03$. In order to compare this result with the ones in M11a, we define the difference in abundance ratio for two elements A and B between the *s*-rich and *s*-poor stars as $\Delta_{\text{poor}}^{\text{rich}} [A/B] \equiv [A/B]_{\text{s-rich}} - [A/B]_{\text{s-poor}}$, we obtain $\Delta_{\text{poor}}^{\text{rich}} [\text{Sr/Fe}] \equiv +0.35 \pm 0.03$. This difference and the mean [Sr/Fe] values for *s*-rich and *s*-poor stars well agree with the ones of the other *n*-capture elements reported in M09 and M11a. Since in the M22 RGB stars the additional content of *n*-capture elements originates from *s*-processes (M11a, Da Costa & Marino 2009, and Roederer et al. 2011), the observed Sr increase in a group of SGB stars must also have a *s*-process origin.

4.2. Barium

In our previous work on RGB M22 stars we have found a bimodality in the Ba abundances (M09 and M11a). However from our analysis on SGB stars, the various Ba abundance distributions shown in Fig. 5 fail to cleanly support the expected bimodality. This is likely due to the larger uncertainty introduced by the high sensitivity of the very strong Ba II 4554 Å line to microturbulent velocity choices and to assumptions about *r/s* isotopic fractions, as discussed in § 3.2. Here we consider just the isotopic dependence.

In the top panel of Fig. 5 we show the Ba abundances derived under assumption that the isotopic ratios are simply those of solar material. The *s*-poor and *s*-rich histograms show very little separation in [Ba/Fe]. In the middle panel we show a more realistic situation by showing LTE Ba abundances computed using a pure *r* isotopic ratio for *s*-poor stars. The mean Ba abundance of the *s*-poor stars decreases from $\log \epsilon(\text{Ba}) = 0.87 \pm 0.02$ ($\langle [Ba/Fe]_{\text{LTE}} \rangle = 0.24 \pm 0.02$, $\sigma = 0.18$) to $\log \epsilon(\text{Ba}) = 0.67 \pm 0.02$ ($\langle [Ba/Fe]_{\text{LTE}} \rangle = 0.04 \pm 0.02$, $\sigma = 0.18$). Finally, in the bottom panel we apply NLTE corrections to the abundances from the middle panel. Clearly there is still significant overlap in *s*-poor and *s*-rich distributions. However, considering just the NLTE Ba abundances, the mean value for the *s*-poor stars is $\log \epsilon(\text{Ba}) = 0.60 \pm 0.02$ ($\langle [Ba/Fe]_{\text{NLTE}} \rangle = -0.03 \pm 0.02$ ($\sigma = 0.16$)). This value is very close to the one obtained for RGB stars by analyzing transitions in the yellow/red spectral regions, $\langle [Ba/Fe] \rangle = -0.05 \pm 0.03$ (Tab. 7 of M11a). The mean Ba content for *s*-rich stars, $\log \epsilon(\text{Ba}) = 1.10 \pm 0.03$ ($\langle [Ba/Fe]_{\text{NLTE}} \rangle = 0.32 \pm 0.03$, $\sigma = 0.22$), also agrees with the RGB value, $\langle [Ba/Fe] \rangle = 0.31 \pm 0.04$ (also Tab. 7 from M11a).

In comparing the Ba and Sr distributions in Fig. 4 and Fig. 5, the less precise results for Ba are apparent. The Ba dispersions

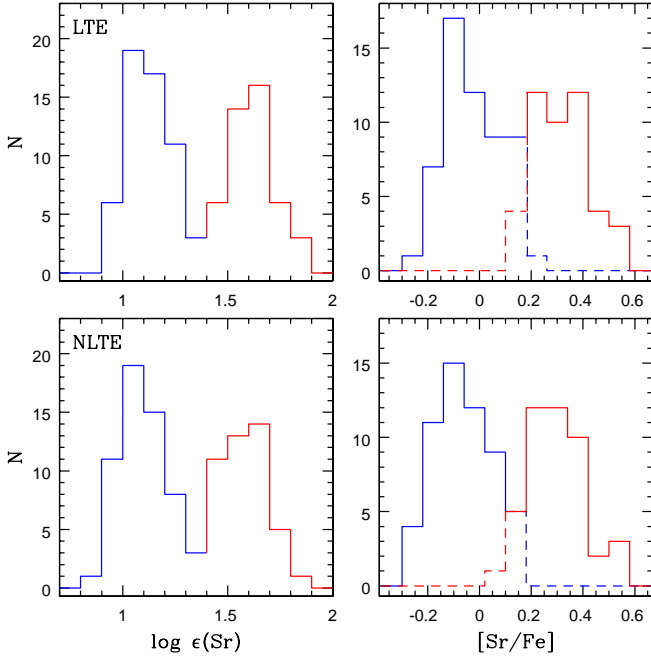


Fig. 4. *Left panels:* Observed distribution of strontium abundances in $\log\epsilon(\text{Sr})$. *Right panels:* Histogram distribution of $[\text{Sr}/\text{Fe}]$ for the stars colored in red and blue in the left histograms. Upper panels show the LTE Sr abundances, lower panels represent the abundances corrected for NLTE effects.

for both s -rich and s -poor stars are much higher than the ones for Sr. But confidence in the basic results for Ba increases by plotting the individual Ba and Sr abundances. We show this in Fig. 6, where our selected s -rich and s -poor stars have been represented with different symbols in the $[\text{Sr}/\text{Fe}]-[\text{Ba}/\text{Fe}]$ and in the $[\text{Sr}/\text{H}]-[\text{Ba}/\text{H}]$ planes. These elements in the solar system are expected to be equally sensitive to s -process nucleosynthesis (see Tab. 10 in Simmerer et al. 2004). In M22 they correlate extremely well on average. In conclusion, we confirm for SGB stars the s -process abundance bimodality found among the RGB stars in M09 and M11a.

4.3. Carbon

Carbon abundances among RGB stars in M22 have been determined by M11a. They found large spread in C content both among s -poor and s -rich stars, with the mean C abundance higher for s -rich stars by 0.35 ± 0.13 . In addition, in each s -group C was found to be anticorrelated with N. This implies that in each s -group, separately, a sub-sample of stars that have undergone high-temperature H burning is present.

We find a large spread of carbon also among the SGB stars. The s -rich stars have significantly larger mean carbon abundances than those of the s -poor stars: $\log\epsilon(\text{C}) = 6.99 \pm 0.03$ ($\langle[\text{C}/\text{Fe}]\rangle = +0.10 \pm 0.03$, $\sigma = 0.23$), while s -poor stars have $\log\epsilon(\text{C}) = 6.67 \pm 0.02$ ($\langle[\text{C}/\text{Fe}]\rangle = -0.07 \pm 0.03$, $\sigma = 0.19$). Thus the abundance difference between the two groups is $\Delta_{\text{poor}}^{\text{rich}}[\text{C}/\text{Fe}] = 0.17 \pm 0.04$, a more than 2σ difference, consistent with the difference found for RGB stars ($\Delta_{\text{poor}}^{\text{rich}}[\text{C}/\text{Fe}] = 0.35 \pm 0.13$, M11a).

To better visualize our results, we computed an average- s -rich and an average- s -poor spectrum by combining stars with very similar atmospheric parameters. The comparison between

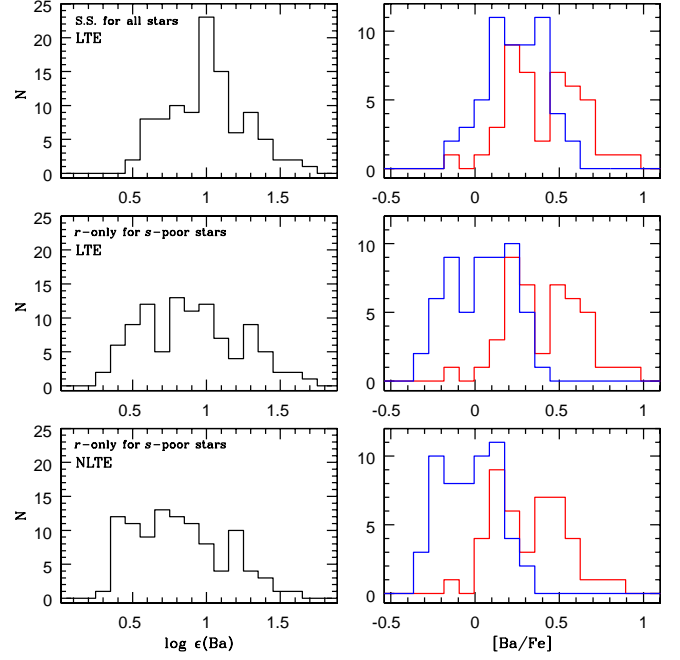


Fig. 5. Observed distribution of Ba in $\log(\epsilon)$ abundances (left panels) and in abundance ratios relative to iron (right panels). The histogram distributions of $[\text{Ba}/\text{Fe}]$ for s -rich and s -poor stars selected as in Fig. 4, have been represented in red and blue respectively. The upper panels represent Ba abundances with Solar System (S.S.) isotopic ratios adopted for both s -rich and s -poor stars. In the middle panels an r -only isotopic ratio has been applied for the s -poor stars. The lower panels represent the same abundances represented in the middle panels corrected for NLTE effects.

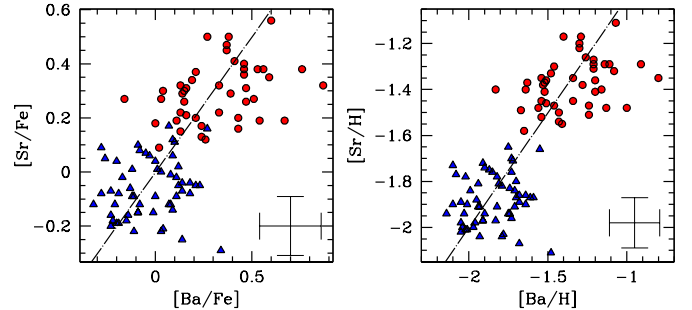


Fig. 6. $[\text{Sr}/\text{Fe}]$ and $[\text{Sr}/\text{H}]$ as a function of $[\text{Ba}/\text{Fe}]$ and $[\text{Ba}/\text{H}]$. s -rich and s -poor stars are plotted in red circles and blue triangles, respectively. The dashed-dotted line represents the perfect agreement.

the two averaged spectra around the spectral features of greatest interest is shown in Fig. 7. The s -rich spectrum (in red) clearly shows stronger Sr, Ba CH features with respect to the s -poor one (in blue). The two available H-lines, shown in the upper panels, show very similar wings, implying that our atmospheric parameters are reasonably correct and the averaged stars have similar parameters.

Note that the mean C abundance among RGB stars (M11a) is ~ 0.5 lower than among SGB stars. This is likely due to the decrease in $[\text{C}/\text{Fe}]$ ratios around the RGB bump ($M_V \sim 0.5$), and can be explained by the onset of a second mixing episode during the red giant evolution of a population II star, once the molecular

weight barrier established by the retreating convective envelope is wiped out by the advancing shell of H-burning (e.g. Sweigart & Mengel 1979; Charbonnel 1995). From that time onward, CN-processed material is able to reach the surface layer, where a decrease of C is visible.

We also see a trend in $[C/Fe]$ with evolutionary phase, as shown in panels (a) and (b) of Fig. 8, where C abundances are plotted as a function of T_{eff} . As a comparison, Sr abundances represented in panels (c) and (d) do not show any trend with T_{eff} . For clarity, we binned abundances in intervals of 200 K in T_{eff} and determined the mean $[C/Fe]$ and $[Sr/Fe]$ abundances for each bin for *s*-rich *s*-poor individually, and for the total sample, as represented by the red, blue and black histograms respectively. To these mean abundances for each bin, we associated the error bars corresponding to the σ divided by $\sqrt{N-1}$, with N being the number of measurements per bin. The red, blue and black error bars in the right corner of panels (a) and (c) represent the σ values for the *s*-rich, *s*-poor, and for the entire sample, respectively.

The carbon rise is particularly pronounced for $T_{\text{eff}} > 6000$ K. The reason for this trend is not clear. For stars with $T_{\text{eff}} > 6000$ K the uncertainties associated to the C abundances are surely higher due to the lower line strengths, and reach values of ~ 0.20 - 0.25 . These uncertainties could have led to a systematic over-estimation of C for the hotter stars. The C rise could also likely be due to our 1D approximation for model atmospheres. A more appropriate analysis of molecular bands should take into account 3D effects that strongly depend on temperature (Collet et al. 2007). However, since this effect appears to be not significantly different between *s*-rich and *s*-poor stars, it does not affect our differential abundance analysis between *s*-rich and *s*-poor stars in M22.

We have already established that the mean value of $[C/Fe]$ is substantially higher for the *s*-rich stars than for the *s*-poor stars over the entire range of SGB T_{eff} . In Fig. 9 the C distribution is represented for the *s*-poor stars (upper panel) and *s*-rich stars (lower panel). The shaded blue and red histograms represent the stars used to construct the average *s*-rich and *s*-poor spectra, while the green ones represent stars with $T_{\text{eff}} > 6000$ K (which show a rise in C with temperature). The distribution of carbon for the two groups of stars suggests the presence of an intrinsic dispersion in C among both *s*-rich and *s*-poor stars. Indeed, both *s*-poor and *s*-rich stars show intrinsic variations of C, N, O, and Na with the presence of N-C and Na-O anticorrelations, as revealed in our high-resolution spectroscopic study on RGBs (M11a). The $[C/Fe]$ abundance dispersion for the *s*-rich and the *s*-poor groups here (σ is 0.23 and 0.19 dex respectively) are marginally larger than the measurement error, which is typically 0.15 dex, and indicate the presence of an intrinsic $[C/Fe]$ spread.

5. The double sub-giant branch of M22

M22 is among the GCs showing a double SGB (Piotto 2009, 2012; M09). In the cluster center the bright SGB component is made up of about 65% of SGB stars while the remaining $\sim 35\%$ of stars defines the fainter SGB component. The multi-wavelength study of M22 from Piotto et al. (2012) reveals that the SGB bimodality is visible in all the bands, from the far ultraviolet (the F275W HST/WFC3 filter) up to the near infrared (the F814W HST/WFC3 filter). These authors also found that the average magnitude difference between the bright SGB and the faint SGB is almost the same at different wavelengths, sug-

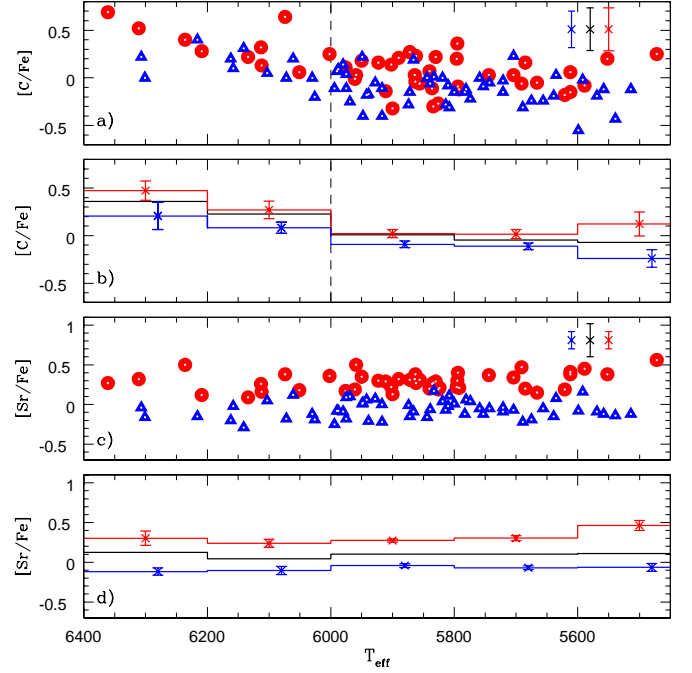


Fig. 8. C and Sr abundance ratios relative to Fe as a function of T_{eff} . In panels (a) and (c) *s*-poor and *s*-rich stars are represented in blue triangles and red circles, respectively. The observed dispersions for *s*-poor, *s*-rich, and the total sample of stars are also shown. In panels (b) and (d) we plot the mean $[C/Fe]$ and $[Sr/Fe]$ values in intervals of 200 K in T_{eff} for the two *s* groups (red and blue lines), and for the total sample (black line).

gesting that the split reflects internal structural properties of the stars, and not only the surface composition.

The RGB of M22 is also made up of two main components, but the RGB split is visible only when appropriate photometric bands are used like the m_1 and the hk Strömrgren indices (Richter et al. 1999, Lee et al. 2009) or the U band (see Fig. 1). While the SGB split is consistent with two stellar groups with either an age difference of ~ 1 - 2 Gyrs, or a difference in their overall C+N+O content, the occurrence of simultaneous RGB and SGB bimodality observed in the $U - V$ color seems to rule out the first hypothesis of a significant age difference (as suggested by Sbordone et al. 2011 for the case of NGC 1851).

M11a have shown that the blue and the red RGB sequences appearing in the I versus m_1 diagram in left panel of Fig. 10 are made of *s*-poor (iron/CNO-poor) and *s*-rich (iron/CNO-rich) stars, respectively. This CMD is a reproduction of the same I versus m_1 diagram of Fig. 19 in M11a, but now we have color-coded in red and blue the stars photometrically belonging to the two RGBs. The same color codes are used to plot these selected stars that are in common with the SUSI photometry, represented in the $U-(U-V)$ CMD (right panel of Fig. 10). In this latter CMD the two RGBs are clearly connected to the two SGBs, providing photometric evidence that the bright SGB and the faint SGB are the sub-giant counterparts of the *s*-poor and *s*-rich RGB, respectively.

Here we can provide direct evidence of the RGBs-SGBs connection, already clear from the CMD inspection, by matching our spectroscopic data on M22 SGB stars with the CMDs where the split is more clearly visible. We remind the reader that our photometry has been corrected for differential reddening effects

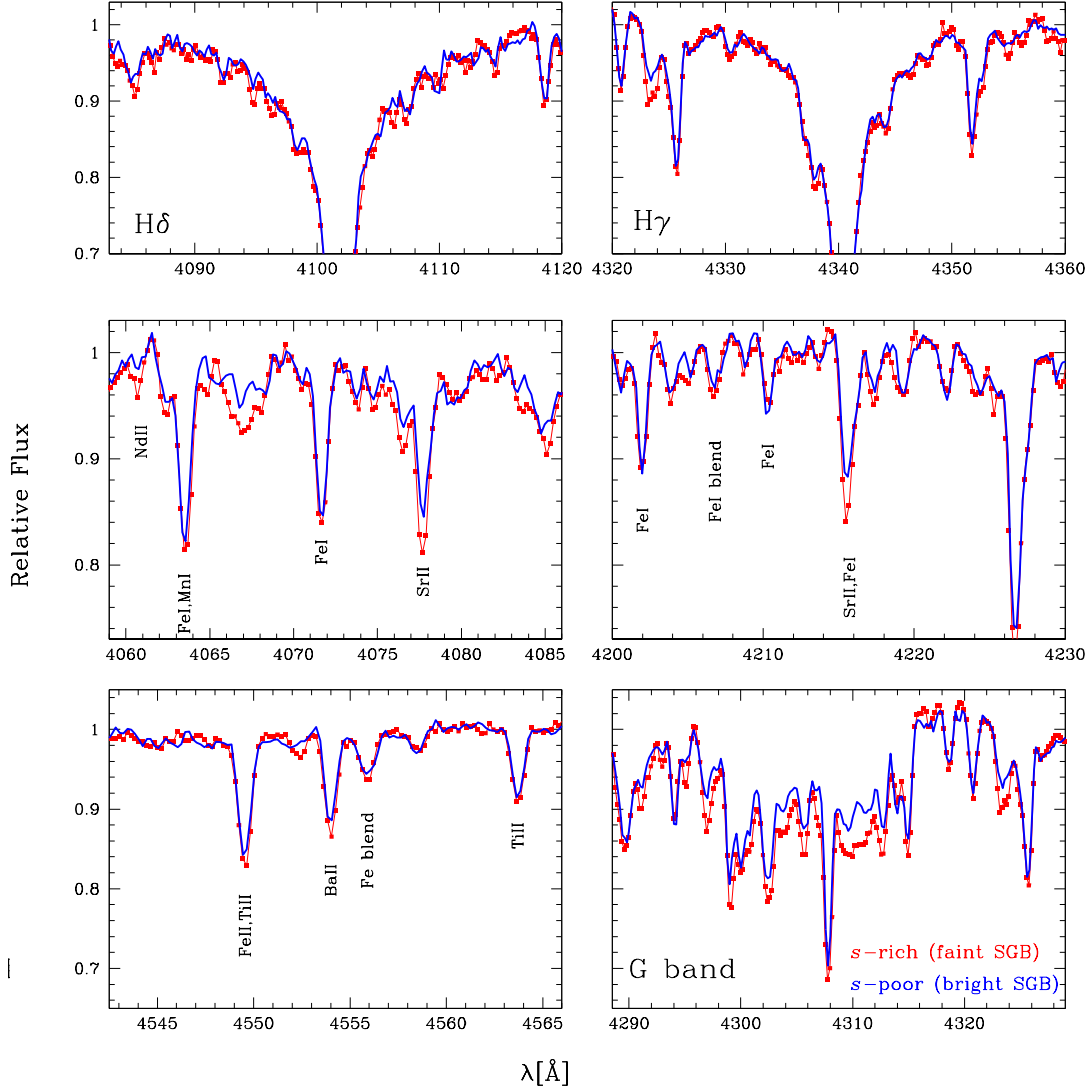


Fig. 7. Combined *s*-poor (blue) and *s*-rich (red) spectra constructed by averaging the spectra for eight *s*-poor stars (#2544, #2207, #2201, #2801, #1913, #735, #3, #768) and eight *s*-rich stars (#1924, #2659, #2153, #2414, #2404, #2099, #2607, #729) with similar atmospheric parameters.

applying the procedure described in Milone et al. (2011, see § 2).

The ground-based and HST CMDs are shown in Fig. 11, with our *s*-rich and *s*-poor stars superimposed. The left panel shows a ground-based $B-(B-V)$ CMD for stars distributed in a large field ($34' \times 33'$) of M22 where we have plotted relatively isolated, unsaturated stars with good values of the PSF-fitting quality index and small σ errors in photometry and astrometry (see Sect. 2.1). The $U-(U-V)$ CMD in the middle panel is from SUSI2 ground-based photometry but covers a small field (two chips of $2.7' \times 5.5'$) in the outskirts of the cluster. The right panel contains the ACS/HST CMD representing stars lying in the most central field ($3' \times 3'$) of the cluster. The double SGB of M22 is clear in all these photometric systems. By coupling our spectroscopic results with these CMDs, it turns out that the *s*-rich stars occupy the fainter SGB, while the *s*-poor ones lie on the upper brighter SGB. All the CMDs of Fig. 11 suggest the same: the *s*-rich and *s*-poor stars segregate along two different branches on the M22 SGB, as predicted by M09. The fact that both the fainter SGB and the redder RGB are made of *s*-rich stars while *s*-poor

stars are located on the brighter SGB and the bluer RGB further confirms the connection between the two RGBs and SGBs.

Our results suggest that: (i) the two SGBs are populated by stars with different *s*-process element content; (ii) the two SGBs “evolve” to the two sequences on the RGB observed in various M22 CMDs and populated by stars with different *s*-process elements, overall metallicity, overall C+N+O, and slightly different Ca, as demonstrated in M11a. Unfortunately, given the moderate resolution of our SGB spectra, we cannot distinguish for SGB stars the small differences in $[\text{Fe}/\text{H}]$ and $[\text{Ca}/\text{Fe}]$ between *s*-rich and *s*-poor stars as found from high resolution spectroscopy on RGB. As found for RGB stars, the SGB *s*-rich and *s*-poor stars have slightly different C abundances, but for SGB stars we have no information on N and O. However, given that we have demonstrated that the two SGBs, in the same way as the two RGBs, have different *s*-process content and C, and that the sequences are photometrically linked, we can fairly extend the results on the two RGBs to the two SGBs for those elements not studied in the present work.

In the light of our results and previous results on the RGB stars by M09 and M11a, we can, for the first time, fully characterize the two SGBs of M22 in terms of chemical composition, as follows:

- faint-SGB: *s*-rich stars, with higher metallicity, Ca and enhanced C+N+O abundance;
- bright-SGB: *s*-poor stars, with lower metallicity, Ca and unenhanced C+N+O abundance;

The chemical properties for the two SGBs are summarized in Tab. 4. For the present discussion we consider calcium and the C+N+O sum as part of the overall metallicity. Thus we take those values determined from RGB high-resolution spectroscopy in M11a, and extend them to the two SGBs with different *s*-process content. As discussed in §4.3, elements like C are highly affected by evolutionary effects that change the surface abundances for stars at different evolutionary stages, however the total C+N+O is not affected by these effects.

Theoretical isochrones can reproduce SGB sequences with different luminosities by assuming an age difference among the two SGB populations. Under this scenario, in M22 the fainter-SGB would be populated by younger stars and the brighter SGB by older ones. If age is assumed to be the lone factor responsible for the M22 SGB split, our isochrones can reproduce the observed separation in magnitude with an age difference of ~ 1 Gyr between the two SGB populations. Of course, this is true only in the case of two stellar populations with identical chemical properties.

However, our results show that there are chemical differences among the two SGBs and hence the scenario of a simple age difference cannot work for this cluster. In particular, the overall C+N+O abundance has a strong impact on isochrones at SGB luminosities. This has fundamental consequences for GC age dating, as demonstrated in recent literature by Cassisi et al. (2008) and D’Antona et al. (2009). For NGC 1851 Cassisi et al. (2008) and Ventura et al. (2009) suggested that the fainter SGB stars could be younger by a few hundred Myrs, if enhanced in the total C+N+O content. Following this scenario large age differences among the two SGBs could be ruled out.

In M22 the SGB *s*-rich stars are distributed along the faint SGB, indicating that the faint SGB is composed of stars enriched in *s*-process elements, and additionally in the total CNO and metallicity, as suggested by our previous study on RGB stars. Here, we use isochrones interpolated in the BASTI database⁷ with the exact CNO and metallicity (determined in our previous work and listed in Tab. 4), to investigate the relative age difference among the *s*-rich and *s*-poor stars. As demonstrated by M09 (see their Fig. 19), isochrones at the same age, and with metallicity different by 0.15 dex (as observed from high resolution spectra), cannot reproduce the entire size of the split. The isochrone fitting accounting for both the metallicity and CNO variation to the SGB region is shown in Fig. 12 for the m_{F606W} versus $m_{F606W} - m_{F814W}$ CMD. The middle blue and red tracks represent the best fitting isochrones to the brighter and the fainter SGB respectively. The age was assumed equal to 13.5 Gyrs which is the value for which the models give the best fit with data. For each of the best-fitting tracks we also show isochrones with the same chemistry but with the age varied by ± 300 Myrs., which is the typical error affecting the determination of relative ages from isochrone fitting. It is clear that, by taking into account the observed difference in the CNO total content, the size of the SGB split is consistent with isochrones of the same age. Note that a

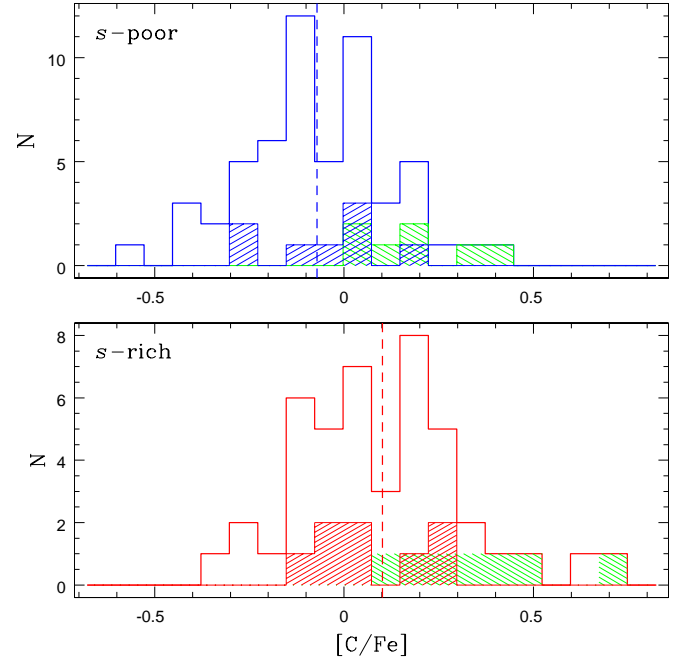


Fig. 9. Carbon abundance relative to Fe distributions for the *s*-poor (upper panel) and *s*-rich (lower panel) stars. In each panel the dashed line represents the mean $[C/Fe]$ abundance. The location of the stars selected for constructing the average *s*-rich and *s*-poor spectrum (see Fig. 7) has been indicated with dashed-red, and blue histograms for *s*-rich and *s*-poor stars respectively. The dashed green histogram represents the location of stars with $T_{\text{eff}} > 6000$ K.

possible He variation (if any), in this range of metallicity and ages, is not expected to change the separation in luminosity between the two SGBs, but only modify the SGB shape (Ventura et al. 2009). From this analysis, the *s*-rich stars appear to be coeval (or possibly slightly younger) than the *s*-poor stars, indicating that star formation in M22 could have developed very rapidly. Possible age differences smaller than ~ 300 Myrs cannot be distinguished by our results.

6. Formation scenarios

In the attempt to understand the chemical and photometric observations in M22, two different scenarios can be basically explored, depending on how different bursts of star formation could have occurred, spatially or temporally separated.

In the first case we may “simply” assume star formation bursts occurred in separated regions that eventually merged together. Then, the *s*-poor and *s*-rich stars could have been formed out of interstellar mediums with slightly different metallicities, and differences in the total C+N+O and *s*-process elements.

If instead, the different bursts of star formation have occurred at different epochs of the cluster evolution, multiple stellar populations in M22 are assumed to be due to self-pollution, with the *s*-rich (metal-richer) stars being the younger population, as they show signatures of pollution from neutron-capture material. As far as we know, the self-pollution hypothesis in M22 would require a number of complex and “fine-tuned” assumptions to reconcile the stellar yields and the lifetimes of possible polluters with the observations (see Sect. 6.1 for more details). Under this scenario, any attempt to identify the responsible polluters should

⁷ www.oa-teramo.inaf.it/BASTI

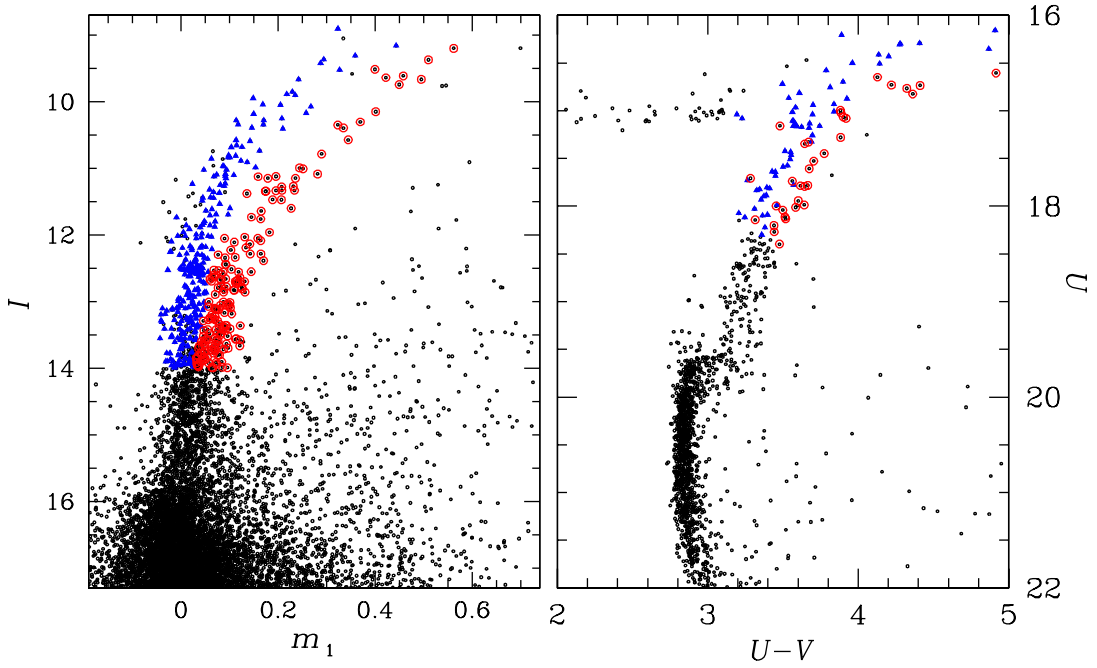


Fig. 10. *Left panel:* I versus the Strömgen index m_1 . Stars belonging to the two RGBs have been represented in red and blue colours. *Right panel:* Stars selected in the double RGB of the I - m_1 diagram, have been represented in the U - $(U - B)$ CMD.

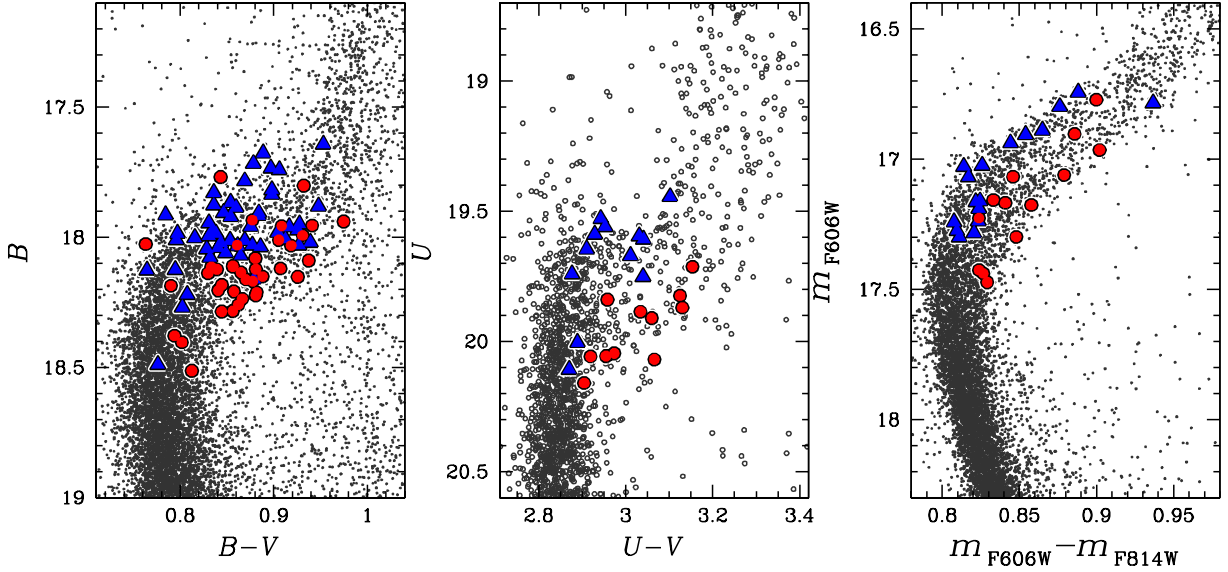


Fig. 11. M22 double SGB in B - $(B - V)$, U - $(U - V)$, and in the m_{F606W} - $(m_{F606W} - m_{F814W})$ CMDs, with the s -rich and s -poor stars superimposed.

take into account the rapid evolution of the cluster, that we have argued on the basis of observational spectroscopic and photometric results coupled with theoretical isochrones.

6.1. Chemical enrichment

Favorable nucleosynthetic sites for the s -process production are AGB stars with $M \leq 3-4M_{\odot}$, which are predicted to experience multiple third dredge-up events (TDU). The number of TDUs decreases for lower mass AGB stars until a minimum mass for which the conditions for the activation of the TDU are never reached. This minimum mass is an increasing func-

tion of metallicity (e.g., Straniero et al. 2003). AGB stars more massive $3-4M_{\odot}$ do not experience many third dredge-up events. They are predicted to pollute the intra-cluster medium only in the p -capture products and, for this reason, have been proposed to be candidate polluters responsible for the light-element (anti)correlations typical of GCs (D'Antona & Caloi 2004). The evolutionary timescale of the less massive AGBs (of order some hundreds of Myrs; see Tab. 1 in Ventura et al. 2009), may be consistent with the uncertainty associated to the null age difference obtained from our isochrones constructed with different CNO contents. However, this still leaves problems in completely accounting for the chemical enrichment history of M22.

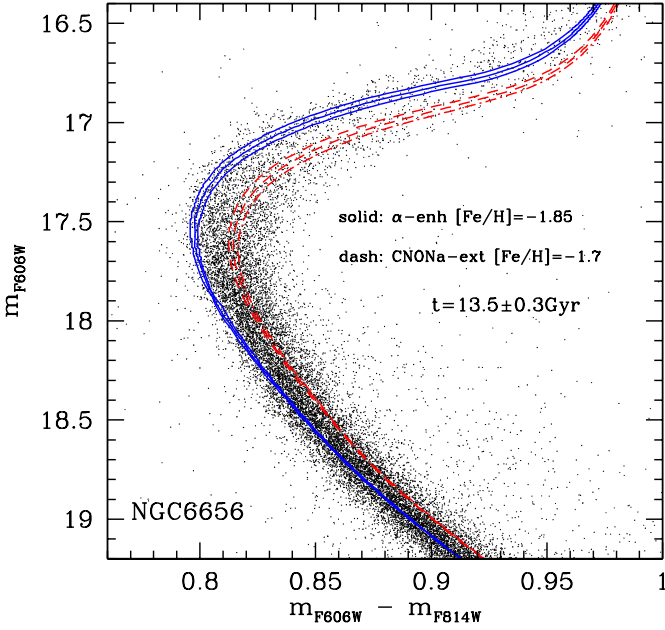


Fig. 12. Isochrones computed with the observed CNO and metallicity of the two s groups, and the same age (13.5 Gyr), superimposed to the M22 SGBs. The red and blue tracks are the CNO-higher (s -rich), and CNO-lower (s -poor) best-fitting isochrones respectively. For both we computed a couple of isochrones with the same chemistry, but with age varied of ± 300 Myrs (dotted tracks).

A primary difficulty is the bimodal metallicity distribution of M22, with the s -rich stars having higher Fe abundances (M09). This suggests that M22 has also undergone enrichment in metallicity, and hence has been likely polluted by yields from Supernovae Type II (SN II, M09).

Moreover, in M22 each s -group individually defines a Na-O anticorrelation, suggesting that both have suffered further enrichment from other polluters, e.g., intermediate-mass AGBs, fast-rotating massive stars, and/or massive binaries. Each of the two M22 s -groups shows its own second-generation enriched in Na and depleted in O (see Fig. 14 in M11a), just like the patterns seen in all the GCs studied so far with sufficient statistics (e.g. Ramírez & Cohen 2002; Carretta et al. 2009). This chemical pattern is difficult to understand. We may speculate that the first stars to form after the first population of metal-poor, s -poor and Na-poor stars, could have been the more metal-rich and s -rich Na-poor stars, as tentatively suggested by Marino et al. (2012) to interpret observations in ω Cen. These two populations could form, at later times, their own Na-O anticorrelation. A similar scenario would require an efficient star formation and the consume of the available intra-cluster material in order to prevent each stellar burst to be contaminated by the preceding one.

A chemical pattern similar to the one observed in M22, even if much more complex, is seen in ω Cen (Johnson & Pilachowski 2010, Marino et al. 2011b; see §1 for more details). For this most peculiar GC D’Antona et al. (2011), compared the Na and O abundances with theoretical AGB yields to account for the presence of the Na-O anticorrelation at different metallicities. They envisaged a chemical evolutionary scenario in which, due to the large mass of ω Cen, the material ejected by SN II could survive in a torus that collapses back onto the cluster after the SN II epoch (see also D’Ercole et al. 2008). The 3D hydro sim-

ulations by Marcolini et al. (2006) show in fact that the collapse back includes the matter enriched by the SN II ejecta. A similar scenario could be tentatively extended to M22.

Alternatively, as observations in GCs strongly suggest that the increase in s -process elements is linked to an increase in Fe, it would be tempting to speculate that s -process elements and Fe may have been produced by the same polluters. Indeed, as outlined in D’Antona et al. (2011), there are other possible sites of s -nucleosynthesis that have not been explored well at present, e.g. the carbon burning shells of lower-mass progenitors of SN II (e.g., The et al. 2007). The pollution from these objects may peculiarly become apparent in the evolution of the progenitor systems of ω Cen and M22.

Interestingly, Roederer et al. (2011) noted that the s -process abundances in the s -rich stars could be more consistent with predictions for more massive AGB stars, those capable of activating the $^{22}\text{Ne}(\alpha, n)^{25}\text{Mg}$ reaction. The main difficulty of this scenario is the lack of a correlation between s -process enrichment and Na within the two groups, which would be expected if these elements are all produced by the same AGB stars of higher masses. However, stars with initial masses $> 3 M_{\odot}$ will evolve in $\lesssim 300$ Myr, which would agree with our derived upper limit on the age difference of the two SGBs in M22. We note here that the efficiency of s -processes depends not just on the number of neutrons but also on the neutron-to-seed nuclei (most likely Fe) ratio. However, the lack of complete grids of theoretical yields for various masses at the exact metallicity of M22 (Cristallo et al. 2011) makes difficult to draw definitive conclusions on the mass of the AGB polluters, in the hypothesis that AGBs are effectively the producers of the extra s -material in M22 s -rich stars. More generally, we admit that the proposed self-pollution channels require an uncomfortable level fine-tunings. The uncertainties, and in some cases the lack, of predicted theoretical yields from different kinds of polluters, introduces further difficulties in interpreting data in the self-pollution framework.

Some of the difficulties encountered by the self-pollution scenario may be overcome invoking a spatial separation (instead than a temporal one) for the different bursts of star formation in a merger scenario. Very recently, dynamical simulations by Bekki & Yong (2011) have shown that it is dynamically plausible that two GCs can merge and form a new GC in the central region of its host dwarf galaxy. The host dwarf galaxy is cannibalized through tidal interactions with the Milky Way and only the compact nucleus survives as a present-day AGC. This scenario has the advantage in explaining in a simple manner the chemical features of the two s -groups of stars in M22 (e.g., their different metallicity and s -process elements content, and the presence of an individual Na-O anticorrelation). However, one still has to understand why the multiple stellar population phenomenon looks similar in all the AGC investigated so far. As an example, both in M22 and NGC 1851 the s -rich stars are slightly enriched in metallicity. In addition if we consider M22 and ω Cen, in both of those clusters the metal-richer and s -richer stars populate fainter SGBs. The occurrence of these similarities may be more easily understood in a self-enrichment scenario. However, note for completeness that the distribution on s -rich and s -poor stars on the SGBs of NGC 1851 could be inverted with respect to M22, as suggested by Carretta et al. (2011), but no direct observations of SGB are currently available for this GC.

At present we are unable to provide a definitive and clear explanation for the M22’s formation and evolution. Both the self-enrichment and the merger scenarios have pro’s and con’s. We only note here that they represent a very different way to interpret M22 and other AGCs. In the first hypothesis they could be

similar to *normal* clusters, but the star formation could have occurred further, and/or owing to their initial higher masses could have retained material escaped from *normal* GCs. In the second hypothesis the AGCs may have been formed through different mechanisms (i.e. a merger) in "exceptional" conditions, most probably in extra-galactic environments.

7. Conclusion

We have presented a medium resolution spectroscopic analysis of a hundred SGB stars in the double-SGB GC M22. The faint SGB is populated by *s*-rich (metal-rich) stars, and the bright SGB by *s*-poor (metal-poor) stars. Our abundance analysis constitutes the first direct evidence for the connection between the two RGBs populated by the two *s*-process stellar groups, discovered in our previous work, and the double SGB. This SGBs-*s*-process connection has also been confirmed by the inspection of the $U-(U-V)$ CMD: the fainter SGB population clearly *evolves* in a redder RGB sequence populated by *s*-rich stars, and the brighter SGB in a bluer branch populated instead by the *s*-poor stars (M11a). Among the RGB stars studied by M11a, the *s*-rich stars are also enhanced in the total CNO, and have a mean higher C with respect to the *s*-poor ones. We can at least extend their conclusion about C and the total CNO to the present SGB sample.

Isochrones constructed with our observed metallicities and C+N+O content for the two *s* groups observed on the RGB suggest that the split SGB is consistent with the two stellar groups being coeval within an uncertainty of ~ 300 Myrs.

Based on our observations, we discussed possible evolutionary histories for the cluster, both in a self-enrichment and in a merger scenario. We underline the difficulties that both scenarios have to overcome and we encourage further investigations on both the theoretical and observational side to finally shed light on the nature of the Milky Way AGCs.

Acknowledgements. We thank F. D'Antona, R. Gratton and C. Allende Prieto for useful comments on the manuscript, and the anonymous referee for his/her suggestions. APM, GP, SC and AA are funded by the Ministry of Science and Technology of the Kingdom of Spain (grant AYA 2010-16717). APM and AA are also funded by the Instituto de Astrofísica de Canarias (grant P3-94). IUR is supported by the Carnegie Institution of Washington through the Carnegie Observatories Fellowship. CS is funded with U.S. National Science Foundation grant AST-0908978. MZ acknowledges the FONDAP Center for Astrophysics 15010003, the BASAL CATA PFB-06, the Milky Way Millennium Nucleus from the Ministry of Economics ICM grant P07-021-F, Proyecto FONDECYT Regular 1110393, and Proyecto Anillo ACT-86 CS

References

- Alonso, A., Arribas, S., & Martínez-Roger, C. 1999, *A&A*, 140, 261
- Anderson, J., & King, I. R. 2006, Instrument Science Report ACS 2006-01, 34 pages, 1
- Anderson, J., Sarajedini, A., Bedin, L. R., et al. 2008, *AJ*, 135, 2055
- Arlandini, C., Käppeler, F., Wisshak, K., Gallino, R., Lugaro, M., Busso, M., & Straniero, O. 1999, *ApJ*, 525, 886
- Bekki, K., & Norris, J. E. 2006, *ApJ*, 637, L109
- Bekki, K., & Yong, D. 2011, arXiv:1109.4463
- Bellini, A., Bedin, L. R., Piotto, G., et al. 2010, *AJ*, 140, 631
- Bergemann, M., & Gehren, T. 2008, *A&A*, 492, 823
- Bergemann, M., et al., to be submitted
- Carretta, E., Bragaglia, A., Gratton, R. G., et al. 2009, *A&A*, 505, 117
- Carretta, E., Gratton, R. G., Lucatello, S., et al. 2010b, *ApJ*, 722, L1
- Carretta, E., Lucatello, S., Gratton, R. G., Bragaglia, A., & D'Orazi, V. 2011, *A&A*, 533, A69
- Casagrande, L., Ramírez, I., Meléndez, J., Bessell, M., & Asplund, M. 2010, *A&A*, 512, A54
- Cassisi, S., Salaris, M., Pietrinferni, A., et al. 2008, *ApJ*, 672, L115
- Castelli, F., & Kurucz, R. L. 2004, arXiv:astro-ph/0405087
- Charbonnel, C. 1995, *ApJ*, 453, L41
- Clampin, M., Sirianni, M., Hartig, G. F., et al. 2002, *Experimental Astronomy*, 14, 107
- Cohen, J. G., Kirby, E. N., Simon, J. D., & Geha, M. 2010, *ApJ*, 725, 288
- Collet, R., Asplund, M., & Trampedach, R. 2007, *A&A*, 469, 687
- Collet, R., Asplund, M., & Nissen, P. E. 2009, *PASA*, 26, 330
- Cristallo, S., Piersanti, L., Straniero, O., et al. 2011, *ApJS*, 197, 17
- Da Costa, G. S., Held, E. V., Saviane, I., & Gullieuszik, M. 2009, *ApJ*, 705, 1481
- Da Costa, G. S., & Marino, A. F. 2011, *PASA*, 28, 28
- D'Antona, F., & Caloi, V. 2004, *ApJ*, 611, 871
- D'Antona, F., Stetson, P. B., Ventura, P., et al. 2009, *MNRAS*, 399, L151
- D'Antona, F., D'Ercole, A., Marino, A. F., et al. 2011, *ApJ*, 736, 5
- Decressin, T., Meynet, G., Charbonnel, C., Prantzos, N., & Ekström, S. 2007, *A&A*, 464, 1029
- de Mink, S. E., Pols, O. R., Langer, N., & Izzard, R. G. 2009, *A&A*, 507, L1
- D'Ercole, A., Vesperini, E., D'Antona, F., McMillan, S. L. W., & Recchi, S. 2008, *MNRAS*, 391, 825
- Dickens, R. J., & Woolley, R. v. d. R. 1967, Royal Greenwich Observatory Bulletins, 128, 255
- Ferraro, F. R., Dalessandro, E., Mucciarelli, A., et al. 2009, *Nature*, 462, 483
- Freeman, K. C., & Rodgers, A. W. 1975, *ApJ*, 201, L71
- Gallagher, A. J., Ryan, S. G., García Pérez, A. E., & Aoki, W. 2010, *A&A*, 523, A24
- Gratton, R., Sneden, C., & Carretta, E. 2004, *ARA&A*, 42, 385
- Gratton, R. G., Carretta, E., & Castellì, F. 1996, *A&A*, 314, 191
- Gray, R. O., & Corbally, C. J. 1994, *AJ*, 107, 742
- Harris, W. E. 1996, *AJ*, 112, 1487
- Hill, V., Plez, B., Cayrel, R., et al. 2002, *A&A*, 387, 560
- Johnson, C. I., & Pilachowski, C. A. 2010, *ApJ*, 722, 1373
- Kappeler, F., Beer, H., & Wisshak, K. 1989, *Reports on Progress in Physics*, 52, 945
- Kraft, R. P. 1994, *PASP*, 106, 553
- Kurucz, R. L. 1992, *The Stellar Populations of Galaxies*, IAU Symp. 149, Dordrecht: Kluwer, 225
- Lee, J.-W., Kang, Y.-W., Lee, J., & Lee, Y.-W. 2009, *Nature*, 462, 480
- Lodders, K. 2003, *ApJ*, 591, 1220
- Mandushev, G., Staneva, A., & Spasova, N. 1991, *A&A*, 252, 94
- Marcolini, A., D'Ercole, A., Brighenti, F., & Recchi, S. 2006, *MNRAS*, 371, 643
- Marino, A. F., Villanova, S., Piotto, G., Milone, A. P., Momany, Y., Bedin, L. R., & Medling, A. M. 2008, *A&A*, 490, 625
- Marino, A. F., Milone, A. P., Piotto, G., et al. 2009, *A&A*, 505, 1099
- Marino, A. F., Sneden, C., Kraft, R. P., et al. 2011a, *A&A*, 532, A8
- Marino, A. F., Milone, A. P., Piotto, G., et al. 2011b, *ApJ*, 731, 64
- Marino, A. F., Milone, A. P., Piotto, G., et al. 2012, *ApJ*, 746, 14
- Mashonkina, L., & Zhao, G. 2006, *A&A*, 456, 313
- Milone, A. P., Bedin, L. R., Piotto, G., et al. 2008, *ApJ*, 673, 241
- Milone, A. P., Stetson, P. B., Piotto, G., et al. 2009, *A&A*, 503, 755
- Milone, A. P., Piotto, G., Bedin, L. R., et al. 2011, *A&A*, in press, arXiv:1108.2391
- Momany, Y., Bedin, L. R., Cassisi, S., et al. 2004, *A&A*, 420, 605
- Norris, J. E., & Da Costa, G. S. 1995, *ApJ*, 447, 680
- Pasquini, L., Avila, G., Blecha, A., et al. 2002, *The Messenger*, 110, 1
- Pasquini, L., Alonso, J., Avila, G., et al. 2003, *Proc. SPIE*, 4841, 1682
- Peterson, R. C., & Cudworth, K. M. 1994, *ApJ*, 420, 612
- Piotto, G. 2009, *IAU Symposium*, 258, 233
- Piotto, G., et al. 2012, submitted to *ApJ*
- Ramírez, S. V., & Cohen, J. G. 2002, *AJ*, 123, 3277
- Richter, P., Hilker, M., & Richtler, T. 1999, *A&A*, 350, 476
- Roederer, I. U., Marino, A. F., & Sneden, C. 2011, *ApJ*, in press, arXiv:1108.3868
- Sbordone, L., Salaris, M., Weiss, A., & Cassisi, S. 2011, *A&A*, 534, A9
- Short, C. I., & Hauschildt, P. H. 2006, *ApJ*, 641, 494
- Simmerer, J., Sneden, C., Cowan, J. J., Collier, J., Woolf, V. M., & Lawler, J. E. 2004, *ApJ*, 617, 1091
- Sirianni, M., Jee, M. J., Benítez, N., et al. 2005, *PASP*, 117, 1049
- Sneden, C. 1973, *ApJ*, 184, 839
- Sollima, A., Ferraro, F. R., Pancino, E., & Bellazzini, M. 2005, *MNRAS*, 357, 265
- Stetson, P. B. 2000, *PASP*, 112, 925
- Stetson, P. B. 2005, *PASP*, 117, 563
- Straniero, O., Domínguez, I., Cristallo, S., & Gallino, R. 2003, *PASA*, 20, 389
- Suntzeff, N. B., & Kraft, R. P. 1996, *AJ*, 111, 1913
- Sweigart, A. V., & Mengel, J. G. 1979, *ApJ*, 229, 624
- The, L.-S., El Eid, M. F., & Meyer, B. S. 2007, *ApJ*, 655, 1058
- Vanbeveren, D., Mennekens, N., & De Greve, J. P. 2011, arXiv:1109.2713
- Ventura, P., Caloi, V., D'Antona, F., et al. 2009, *MNRAS*, 399, 934
- Ventura, P., D'Antona, F., Mazzitelli, I., & Gratton, R. 2001, *ApJ*, 550, L65
- Yong, D., Grundahl, F., Johnson, J. A., & Asplund, M. 2008, *ApJ*, 684, 1159

Yong, D., & Grundahl, F. 2008, ApJ, 672, L29

Yong, D., Grundahl, F., D'Antona, F., et al. 2009, ApJ, 695, L62

Table 1. Ground-based photometric database.

Telescope	Dates	Camera
ESO Dutch 0.91m	1997 Apr 12-16	CCD Tektronix
CTIO 0.9m	1998 Apr 16-22	CCD Tek2K_3
CTIO 0.9m	1991 Sep 18-29	CCD 772
JKT 1.0m	1998 Jun 20-26	CCD TEK4
ESO NTT 3.6m	1993 Jul 15-23	EMMI+Tektronix
ESO NTT 3.6m	1993 May 30-31	SUSI2+EEV44-80
ESO/MPI 2.2m	2002 Jun 17-21	WFI
ESO/MPI 2.2m	1999 May 12-15	WFI
ESO/MPI 2.2m	2000 Jul 06-12	WFI
ESO/MPI 2.2m	1999 Jul 06 12	WFI
ESO/MPI 2.2m	2004 Jun 13-28	WFI

Table 2. M22 targets: positions, and photometric data.

ID ^a	$\alpha(2000)$	$\delta(2000)$	U^b	B^c	V^c	I^c	$\Delta E(B - V)^d$
3	18:35:45.23	-23:52:23.7	99.999	18.016	17.159	16.049	-0.004
24	18:35:53.65	-23:58:04.5	99.999	17.943	17.125	16.053	-0.013
77	18:36:01.27	-23:55:38.0	99.999	17.845	16.976	15.839	-0.015
94	18:36:02.73	-23:53:24.6	99.999	18.207	17.330	16.170	-0.004
99	18:36:03.12	-23:52:33.1	99.999	18.082	17.249	15.983	0.001
112	18:36:04.09	-23:49:31.0	99.999	18.091	17.235	16.129	0.007
151	18:36:06.55	-23:55:03.2	99.999	17.937	17.102	16.029	-0.019
221	18:36:10.54	-23:56:42.5	99.999	17.981	17.116	15.969	-0.012
254	18:36:12.08	-23:51:11.8	99.999	18.053	17.225	16.114	0.012
262	18:36:12.62	-23:50:02.4	99.999	17.998	17.160	16.044	-0.006
263	18:36:12.59	-23:55:48.8	19.689	17.875	16.916	15.704	-0.016
268	18:36:12.79	-23:52:57.5	19.857	18.130	17.247	16.089	-0.005
277	18:36:12.95	-23:56:02.8	19.743	17.943	17.046	15.861	-0.016
290	18:36:13.28	-23:52:31.0	19.773	17.983	17.035	15.822	0.007
292	18:36:13.36	-23:53:57.7	99.999	17.756	16.873	15.738	-0.015
298	18:36:13.56	-23:54:27.0	19.615	17.912	17.064	15.984	0.002
312	18:36:14.05	-23:52:21.4	19.388	17.656	16.700	15.466	0.003
329	18:36:14.48	-23:54:58.0	99.999	17.842	16.967	15.839	0.006
351	18:36:15.08	-23:57:01.1	19.907	18.049	17.159	16.002	-0.017
352	18:36:15.08	-23:56:41.3	20.048	18.263	17.424	16.339	-0.006
374	18:36:15.60	-23:58:31.5	99.999	17.796	16.913	15.737	-0.043
375	18:36:15.62	-23:55:28.1	20.054	18.299	17.439	16.227	0.004
398	18:36:16.25	-23:52:33.1	19.538	17.844	16.905	15.704	-0.009
456	18:36:17.09	-23:54:07.9	19.567	17.675	16.787	15.624	-0.001
472	18:36:17.48	-23:54:45.0	20.040	18.267	17.448	16.391	0.011
479	18:36:17.53	-23:50:30.3	99.999	18.154	17.280	16.140	-0.004
494	18:36:17.73	-23:49:41.6	99.999	18.129	17.237	16.094	0.012
557	18:36:18.40	-23:53:04.0	20.021	18.167	17.330	16.192	0.007
575	18:36:18.60	-23:54:30.1	99.999	18.416	17.613	16.572	0.009
614	18:36:18.93	-23:52:19.1	19.784	18.035	17.111	15.923	-0.013
718	18:36:19.90	-23:53:55.4	99.999	17.543	16.735	15.660	0.011
725	18:36:19.96	-23:54:34.8	20.168	18.546	17.756	16.732	0.014
729	18:36:20.00	-23:53:00.5	20.079	18.295	17.424	16.264	0.009
735	18:36:20.03	-23:56:28.4	19.602	17.883	17.024	15.900	-0.001
768	18:36:20.25	-23:56:01.4	19.684	17.934	17.046	15.897	0.004
810	18:36:20.53	-23:55:28.2	99.999	18.079	17.303	15.738	0.013
911	18:36:21.19	-23:53:32.6	99.999	17.974	17.175	16.149	0.014
972	18:36:21.56	-23:53:48.4	99.999	17.574	16.724	15.633	0.003
975	18:36:21.56	-23:56:46.8	19.864	18.116	17.259	16.131	0.001
993	18:36:21.69	-23:52:30.8	20.137	18.486	17.664	16.568	0.020
1037	18:36:21.93	-23:55:38.6	19.589	17.891	17.040	15.876	0.015
1110	18:36:22.40	-23:52:25.6	19.578	17.823	16.919	15.758	0.026
1114	18:36:22.41	-23:54:37.2	99.999	18.548	17.727	16.644	0.009
1116	18:36:22.42	-23:53:41.5	99.999	17.951	17.017	15.795	0.001
1138	18:36:22.58	-23:57:08.0	99.999	17.847	16.904	15.721	0.011
1257	18:36:23.35	-23:55:33.9	99.999	18.212	17.396	16.320	0.021
1289	18:36:23.59	-23:52:38.9	19.680	18.019	17.141	16.041	0.024
1451	18:36:24.56	-23:54:56.1	99.999	18.267	17.411	16.287	0.015

Table 2. continued.

ID ^a	$\alpha(2000)$	$\delta(2000)$	U^b	B^c	V^c	I^c	$\Delta E(B - V)^d$
1526	18:36:24.98	-23:52:37.8	99.999	18.058	17.243	16.167	0.018
1637	18:36:25.65	-23:54:31.7	99.999	18.351	17.379	16.323	0.020
1663	18:36:25.84	-23:52:35.9	99.999	18.032	17.184	16.083	0.013
1685	18:36:26.06	-23:54:21.2	99.999	17.710	16.871	15.774	0.018
1763	18:36:26.68	-23:54:59.2	99.999	18.346	17.525	16.404	0.019
1792	18:36:26.86	-23:54:36.4	99.999	18.102	17.200	16.178	0.016
1821	18:36:27.09	-23:52:14.3	99.999	18.203	17.314	16.177	0.010
1894	18:36:27.53	-23:53:53.2	99.999	18.062	17.219	16.117	0.017
1903	18:36:27.61	-23:58:00.7	99.999	17.924	17.125	16.039	-0.030
1913	18:36:27.69	-23:55:08.4	99.999	17.840	16.941	15.797	0.025
1924	18:36:27.74	-23:53:19.0	99.999	17.975	17.088	15.967	0.010
1939	18:36:27.85	-23:54:12.7	99.999	17.920	17.053	15.982	0.013
1988	18:36:28.26	-23:54:50.2	99.999	18.276	17.464	16.340	0.022
1993	18:36:28.29	-23:55:40.3	99.999	18.075	17.146	15.937	0.010
2061	18:36:29.01	-23:53:35.4	99.999	17.905	17.139	16.071	0.016
2099	18:36:29.36	-23:56:09.2	99.999	18.140	17.274	16.152	0.001
2153	18:36:29.78	-23:52:55.4	99.999	18.103	17.238	16.141	-0.006
2161	18:36:29.88	-23:59:04.3	99.999	17.965	17.085	15.964	-0.046
2175	18:36:30.02	-23:55:48.1	99.999	18.173	17.280	16.131	0.012
2201	18:36:30.25	-23:52:25.5	99.999	18.043	17.175	16.083	-0.003
2207	18:36:30.28	-23:50:34.8	99.999	17.808	16.933	15.778	0.006
2209	18:36:30.28	-23:55:33.5	99.999	18.224	17.391	16.298	0.014
2242	18:36:30.65	-23:58:20.9	99.999	17.978	17.178	16.073	-0.033
2278	18:36:30.98	-23:53:59.7	99.999	17.888	17.049	15.968	0.003
2300	18:36:31.14	-23:52:20.6	99.999	17.999	17.206	16.150	-0.003
2312	18:36:31.32	-23:52:58.3	99.999	17.776	16.931	15.882	0.002
2318	18:36:31.35	-23:53:47.8	99.999	17.979	17.140	16.085	0.008
2321	18:36:31.41	-23:57:44.3	99.999	17.664	16.777	15.621	-0.019
2334	18:36:31.55	-23:53:12.0	99.999	17.980	17.066	15.937	0.006
2353	18:36:31.69	-23:53:25.8	99.999	18.150	17.380	16.373	0.006
2364	18:36:31.92	-24:00:17.7	99.999	17.860	16.960	15.792	-0.039
2391	18:36:32.50	-23:55:37.5	99.999	17.917	16.999	15.796	0.020
2404	18:36:32.70	-24:01:01.7	99.999	18.087	17.257	16.152	-0.036
2414	18:36:33.06	-23:57:10.2	99.999	18.165	17.294	16.189	0.001
2419	18:36:33.20	-23:57:58.6	99.999	17.985	17.141	16.058	-0.021
2421	18:36:33.27	-23:50:13.8	99.999	18.108	17.252	16.065	-0.000
2481	18:36:34.86	-23:50:30.7	99.999	18.039	17.199	16.090	-0.000
2505	18:36:35.65	-23:57:57.9	99.999	18.136	17.303	16.210	-0.012
2542	18:36:36.81	-23:55:46.6	99.999	18.041	17.105	15.882	0.019
2544	18:36:36.85	-23:50:25.1	99.999	18.004	17.137	15.998	-0.002
2570	18:36:38.23	-23:51:12.5	99.999	17.961	17.133	16.012	-0.005
2572	18:36:38.33	-23:52:51.0	99.999	18.001	17.159	16.065	0.004
2590	18:36:39.01	-23:58:07.9	99.999	18.043	17.113	15.888	0.003
2607	18:36:39.89	-23:54:02.5	99.999	18.264	17.393	16.267	0.014
2621	18:36:40.64	-23:54:20.6	99.999	18.030	17.090	15.884	0.009
2625	18:36:41.07	-23:51:22.1	99.999	18.049	17.228	16.109	-0.018
2650	18:36:42.62	-23:52:49.9	99.999	18.058	17.141	15.996	0.012
2659	18:36:43.23	-23:53:19.0	99.999	18.080	17.207	16.078	0.012
2669	18:36:44.22	-23:48:31.5	99.999	17.976	17.073	15.897	-0.001
2672	18:36:44.63	-23:49:45.3	99.999	17.783	16.874	15.697	0.012
2689	18:36:45.66	-23:54:21.6	99.999	18.274	17.377	16.209	0.015
2801	18:36:59.22	-23:52:16.7	99.999	17.913	17.049	15.914	-0.011
2815	18:37:03.73	-23:49:56.7	99.999	17.932	17.009	15.824	-0.004

^(a) Identification numbers come from the ground-based photometric catalog described in Sect. 2.1 ^(b) Momany et al. (2004) photometric data-base. ^(c) Stetson photometric data-base. ^(d) Differential reddening correction values for each target star.

Table 3. M22 C, Sr, Ba abundances for SGB stars. The standard deviation σ_{Sr} for the two Sr lines and the *s*-group are also listed for each star.

ID	T_{eff}	$\log g$	[Sr/Fe]	σ_{Sr}	[Ba/Fe]	[C/Fe]	<i>s</i> -group ^a
3	5866	3.88	-0.09	0.12	-0.12	0.19	<i>s</i> -poor
24	5942	3.92	0.06	0.14	0.09	-0.18	<i>s</i> -poor
77	5774	3.78	0.04	0.21	0.00	-0.22	<i>s</i> -poor
94	5794	3.92	0.40	0.11	0.46	-0.09	<i>s</i> -rich
99	6026	3.96	-0.19	0.07	-0.19	-0.20	<i>s</i> -poor
112	5917	3.92	-0.00	0.13	0.03	-0.40	<i>s</i> -poor
151	5872	3.89	-0.15	0.06	-0.09	-0.15	<i>s</i> -poor
221	5808	3.85	0.11	0.05	0.10	-0.31	<i>s</i> -poor
254	6030	3.96	-0.12	0.03	-0.21	0.00	<i>s</i> -poor
262	5939	3.91	-0.21	0.05	0.04	-0.17	<i>s</i> -poor
263	5472	3.62	0.56	0.00	0.60	0.25	<i>s</i> -rich
268	5744	3.87	0.37	0.09	0.21	0.03	<i>s</i> -rich
277	5689	3.77	-0.22	0.06	0.03	-0.31	<i>s</i> -poor
290	5552	3.69	0.38	0.11	0.46	0.20	<i>s</i> -rich
292	5743	3.72	-0.05	0.11	0.21	-0.05	<i>s</i> -poor
298	5928	3.86	0.07	0.02	-0.05	-0.05	<i>s</i> -poor
312	5514	3.54	-0.12	0.01	0.07	-0.12	<i>s</i> -poor
329	5834	3.78	0.27	0.01	0.03	-0.30	<i>s</i> -rich
351	5685	3.82	0.20	0.20	0.43	0.16	<i>s</i> -rich
352	5911	4.01	0.29	0.04	0.14	-0.14	<i>s</i> -rich
374	5592	3.73	0.16	0.18	0.27	-0.02	<i>s</i> -poor
375	5900	3.99	0.13	0.02	0.24	-0.32	<i>s</i> -rich
398	5558	3.65	-0.12	0.01	-0.08	-0.12	<i>s</i> -poor
456	5753	3.68	-0.12	0.01	0.08	-0.09	<i>s</i> -poor
472	6103	4.06	0.05	0.00	-0.26	0.05	<i>s</i> -poor
479	5792	3.90	0.21	0.01	0.16	-0.12	<i>s</i> -rich
494	5796	3.86	0.22	0.18	0.13	0.20	<i>s</i> -rich
557	6002	3.98	0.36	0.12	0.46	0.25	<i>s</i> -rich
575	6236	4.16	0.50	0.04	0.27	0.40	<i>s</i> -rich
614	5589	3.75	0.45	0.04	0.37	-0.08	<i>s</i> -rich
718	6134	3.79	0.09	0.16	0.02	0.22	<i>s</i> -rich
725	6301	4.24	-0.16	0.07	-0.23	0.00	<i>s</i> -poor
729	5864	3.97	0.32	0.04	0.13	0.03	<i>s</i> -rich
735	5874	3.82	-0.01	0.08	0.08	-0.28	<i>s</i> -poor
768	5759	3.79	-0.05	0.04	0.12	0.00	<i>s</i> -poor
810	6311	4.08	0.32	0.07	0.87	0.52	<i>s</i> -rich
911	6216	3.99	-0.15	0.00	-0.09	0.40	<i>s</i> -poor
972	5949	3.72	0.01	0.08	-0.12	0.22	<i>s</i> -poor
975	5890	3.92	0.32	0.08	0.33	0.21	<i>s</i> -rich
993	6112	4.15	0.16	0.04	0.43	0.13	<i>s</i> -rich
1037	5980	3.85	-0.09	0.01	0.11	0.14	<i>s</i> -poor
1110	5800	3.72	0.01	0.23	0.01	-0.15	<i>s</i> -poor
1114	6113	4.17	0.26	0.03	0.15	0.32	<i>s</i> -rich
1116	5639	3.71	-0.15	0.04	-0.01	-0.19	<i>s</i> -poor
1138	5612	3.65	0.41	0.14	0.41	0.06	<i>s</i> -rich
1257	6162	4.05	-0.20	0.07	-0.23	0.20	<i>s</i> -poor
1289	5781	3.81	0.06	0.05	-0.03	-0.12	<i>s</i> -poor
1451	5950	3.99	0.35	0.09	0.59	0.18	<i>s</i> -rich
1526	6141	3.99	-0.29	0.09	0.34	0.31	<i>s</i> -poor
1637	5539	3.80	-0.14	0.04	0.09	-0.43	<i>s</i> -poor
1663	5988	3.91	-0.08	0.08	0.18	0.09	<i>s</i> -poor
1685	6051	3.80	0.18	0.12	0.00	0.06	<i>s</i> -rich
1763	6072	4.09	-0.18	0.05	-0.15	0.00	<i>s</i> -poor
1792	5783	3.83	-0.12	0.23	-0.32	-0.15	<i>s</i> -poor
1821	5824	3.90	0.21	<i>s</i> -rich
1894	6074	3.94	0.38	0.06	0.56	0.64	<i>s</i> -rich
1903	5975	3.95	0.09	0.11	-0.28	-0.11	<i>s</i> -poor
1913	5810	3.73	-0.02	0.16	0.11	-0.08	<i>s</i> -poor
1924	5856	3.81	0.31	0.11	0.47	-0.06	<i>s</i> -rich
1939	5917	3.83	-0.22	0.11	-0.11	-0.11	<i>s</i> -poor
1988	6209	4.09	0.12	0.20	0.26	0.28	<i>s</i> -rich
1993	5691	3.77	0.47	0.02	0.37	-0.06	<i>s</i> -rich
2061	6361	4.03	0.27	0.00	-0.16	0.69	<i>s</i> -rich
2099	5862	3.91	0.27	0.10	0.51	0.23	<i>s</i> -rich
2153	5840	3.90	0.20	0.15	0.21	0.07	<i>s</i> -rich
2161	5612	3.80	0.38	0.07	0.76	-0.15	<i>s</i> -rich
2175	5795	3.88	0.30	0.23	0.04	0.36	<i>s</i> -rich

Table 3. continued.

ID	T _{eff}	log <i>g</i>	[Sr/Fe]	σ_{Sr}	[Ba/Fe]	[C/Fe]	<i>s</i> -group ^a
2201	5833	3.87	0.17	0.23	0.07	0.01	<i>s</i> -poor
2207	5819	3.76	0.04	0.20	-0.20	0.00	<i>s</i> -poor
2209	6061	4.02	0.12	0.08	0.09	0.20	<i>s</i> -poor
2242	5959	3.97	0.50	0.04	0.38	0.03	<i>s</i> -rich
2278	5975	3.87	-0.18	0.08	-0.22	0.04	<i>s</i> -poor
2300	6158	4.00	-0.02	0.01	-0.17	0.10	<i>s</i> -poor
2312	5976	3.81	0.17	0.19	0.24	0.11	<i>s</i> -rich
2318	5990	3.90	-0.08	0.06	-0.28	0.07	<i>s</i> -poor
2321	5675	3.67	-0.19	0.05	-0.20	-0.24	<i>s</i> -poor
2334	5704	3.76	0.34	0.10	0.19	0.03	<i>s</i> -rich
2353	6307	4.12	-0.04	0.03	0.14	0.22	<i>s</i> -poor
2364	5569	3.72	-0.09	0.04	0.00	-0.19	<i>s</i> -poor
2391	5704	3.73	-0.07	0.07	0.14	0.23	<i>s</i> -poor
2404	5836	3.95	0.26	0.09	0.47	-0.11	<i>s</i> -rich
2414	5830	3.91	0.29	0.01	0.39	0.22	<i>s</i> -rich
2419	5844	3.89	-0.16	0.04	-0.14	0.00	<i>s</i> -poor
2421	5902	3.92	0.22	0.18	0.33	0.14	<i>s</i> -rich
2481	5948	3.92	0.02	0.22	0.12	-0.40	<i>s</i> -poor
2505	5923	3.97	0.30	0.01	0.15	0.16	<i>s</i> -rich
2542	5656	3.74	-0.05	0.01	0.23	-0.24	<i>s</i> -poor
2544	5839	3.86	-0.06	0.09	-0.13	-0.06	<i>s</i> -poor
2570	5994	3.92	-0.25	0.12	0.14	-0.11	<i>s</i> -poor
2572	5969	3.91	0.10	0.06	-0.09	-0.25	<i>s</i> -poor
2590	5599	3.75	-0.08	0.05	-0.19	-0.55	<i>s</i> -poor
2607	5872	3.96	0.31	0.01	0.16	0.27	<i>s</i> -rich
2621	5621	3.73	0.19	0.12	0.67	-0.18	<i>s</i> -rich
2625	5961	3.96	0.19	0.14	0.54	-0.01	<i>s</i> -rich
2650	5666	3.78	0.15	0.21	0.13	-0.05	<i>s</i> -rich
2659	5863	3.88	0.38	0.04	0.53	-0.04	<i>s</i> -rich
2669	5721	3.78	-0.04	0.12	0.18	-0.03	<i>s</i> -poor
2672	5721	3.69	-0.09	0.04	-0.11	-0.15	<i>s</i> -poor
2689	5826	3.91	0.19	0.01	0.11	-0.27	<i>s</i> -rich
2801	5814	3.82	-0.07	0.03	-0.23	-0.28	<i>s</i> -poor
2815	5635	3.72	0.08	0.03	-0.08	0.03	<i>s</i> -poor

^(a) Global metallicities of [A/H]=-1.82 and [A/H]=-1.67 were employed for *s*-poor and *s*-rich stars, respectively (see § 3.1 for more details).

Table 4. Chemical features of the two M22 SGB. The [Fe/H] and the CNO total content are the values determined by Marino et al. (2011) for RGB stars.

	[Fe/H] ^a	σ	[C+N+O/Fe] ^a	σ	[C/Fe]	σ	[Sr/Fe]	σ	[Ba/Fe]	σ
SGB-faint	-1.67±0.01	0.05	+0.41±0.02	0.07	+0.10±0.03	0.23	+0.29±0.02	0.11	+0.32±0.03	0.22
SGB-bright	-1.82±0.02	0.07	+0.28±0.02	0.09	-0.07±0.03	0.19	-0.06±0.01	0.11	-0.03±0.02	0.16

^a For these two columns values obtained from RGB stars in Marino et al. (2009, 2011) are listed.